Braids in the heart (Supplement)

Global measures of mixing for cardiovascular flows

Di Labbio G[1†], Thiffeault J-L[2], Kadem L[3]
[1] *Département de génie mécanique, École de technologie supérieure, Montréal, QC H3C 1K3, Canada*
[2] *Department of Mathematics, University of Wisconsin – Madison, Madison, WI 53706, USA*
[3] *Laboratory of Cardiovascular Fluid Dynamics, Concordia University, Montréal, QC H3G 1M8, Canada*

In this supplementary information, we provide additional details on the basic theory of braids and on the convergence behaviour of the braid properties of interest. We also extend discussions regarding the fraction of pseudo-Anosov braids and the normalization method of the braid writhe. Lastly, we define the expressions for the non-braid-related quantities used in the main text, namely, measures of the circulation, the energy dissipation index and the finite-time Lyapunov exponent.

I. Some basics of braids

In this section, we aim to equip the reader with a basic working knowledge of braid theory in the context of particle trajectories in fluid flows. We describe only the essential concepts in this document as our objective in the main text is primarily to demonstrate how braids are useful to the cardiovascular flow community. For more detailed information on the theory of braids, we instead refer the reader to Artin (1947), Birman (1975), Thiffeault (2005, 2010), Thiffeault and Finn (2006), Allshouse and Thiffeault (2012) and Budišić and Thiffeault (2015). For recent interesting applications, we refer the reader to Francois et al. (2016) and Filippi et al. (2020).

A. Topological representation of particle trajectories using braids

Translation of particle trajectories to braids. Let us begin from the same example as in Fig. 2 of the main text, reproduced here as Fig. S.1 for convenience. Consider a few particles moving about in a two-dimensional flow as in Fig. S.1*a*. If we augment the plane of motion with time so as to view the world lines of the particles, as in Fig. S.1*b*, the particle trajectories clearly become entangled in time. This entangled plot of particle trajectories forms a 'physical braid' with the trajectories themselves serving as the strands of the braid. Figure S.1*c* shows a normalized form of the physical braid, called a 'braid diagram', which is a convenient way of keeping track of the crossings between particles, specifically the times (and order) at which the crossings occur and which particle is crossing 'over' or 'under' the other. A braid can therefore express particle trajectories in a topological sense, namely, in a world where two objects are equivalent so long as they can be continuously deformed into each other without passing through themselves. The crossing information of the trajectories is effectively encoded in the braid. Strictly speaking, braid theory can only be applied in the context of two-dimensional flows. Two-dimensional particle trajectories form braids in three dimensions when viewed as a space-time diagram (as in Fig. S.1). Likewise, three-dimensional particle trajectories form braids in four dimensions. All braids in four or more dimensions are trivial (i.e., they can all be 'undone', cf. Birman (1975)).

Determination of the type of crossing (over or under). In order to define whether a particle crosses over or under another in the braid diagram, we project the particle positions onto an arbitrary projection line, which may have some elevation angle (α), and number the particle positions according to the order of their projection. A particle that passes in front of the other produces an over crossing and one that passes behind produces an under

† **Email address for correspondence:** giuseppe.dilabbio@etsmtl.ca

crossing. For example, Fig. S.2 shows two particles, one black and the other white, with the former moving around the latter. In Fig. S.2*a*, when viewed from below ($\alpha = 0$), the black particle is the first to be projected and it moves behind the white particle. Consequently, the corresponding braid diagram shows the first strand woven under the second. When viewed from the side ($\alpha = \pi/2$), the black particle is now the second to be projected and it moves in front of the white particle. Consequently, the corresponding braid diagram shows the second strand woven over the first. Either way, although the projected order of the particles has changed when viewed from $\alpha = 0$ or $\pi/2$, the resulting crossing in the braid diagram is the same. The opposite scenario is shown in Fig. S.2*b*.

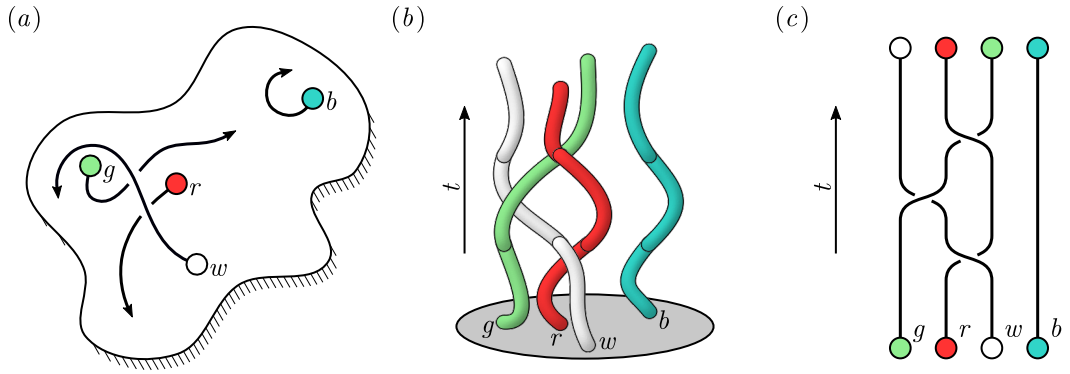

Figure S.1: (*a*) Schematic of four coloured particles (green, red, white and blue labelled g, r, w and b respectively) moving in a two-dimensional flow. (*b*) The corresponding world lines of the particles (the vertical axis being time, t) forming a physical braid. (*c*) The associated braid diagram with time again increasing from bottom to top. The corresponding 'braid word' is $\sigma_2\sigma_1^{-1}\sigma_2$, where here we use the convention that a braid word read from left to right represents the braid from bottom to top (i.e., forward in time). The 'length' of the braid corresponds to the number of crossings in the braid diagram or, alternatively, to the absolute sum of the exponents in the braid word (i.e., $L = |1| + |-1| + |1| = 3$). The 'writhe' of the braid, on the other hand, simply corresponds to the sum of the exponents in the braid word (i.e., $\mathrm{Wr} = 1 - 1 + 1 = 1$).

Representation of a braid algebraically using generators. Let us denote the crossing of strand i under strand $i+1$, representing a clockwise interchange of particles (as in Fig. S.2*a*), by the symbol σ_i and the crossing of strand i over strand $i+1$, representing a counterclockwise interchange (as in Fig. S.2*b*), by the symbol σ_i^{-1}. In so doing, we can express the braid in an algebraic manner. The elementary symbols σ_i and σ_i^{-1} are known as the generators of the Artin n-braid group ($\mathcal{B}_n$, n being the number of strands in the braid). The binary operation of the group

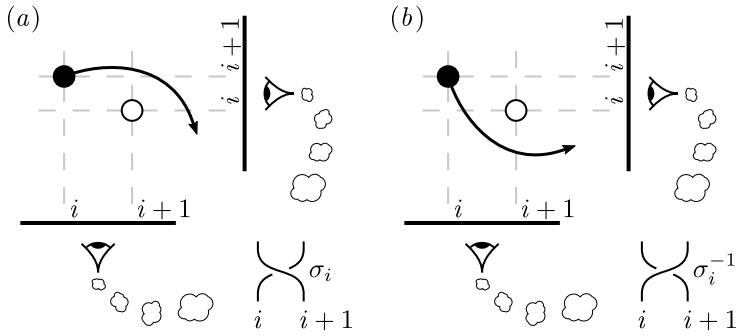

Figure S.2: Schematic demonstrating the translation of particle trajectories to a braid diagram. (*a*) A clockwise interchange of particles produces an 'under' braid, with the first strand woven under the second (braid generator σ_i). (*b*) A counterclockwise interchange of particles produces an 'over' braid, with the first strand woven over the second (braid generator σ_i^{-1}).

is composition (or concatenation) where $\sigma_i\sigma_j$ would mean to append the σ_j generator on top of the σ_i generator. So, for example, the 'braid word' corresponding to Fig. S.1*c* is $\sigma_2\sigma_1^{-1}\sigma_2$, where here we choose the convention that a braid word read from left to right represents the braid from bottom to top (i.e., forward in time). It is rather easy to verify that the group axioms are all satisfied (i.e., closure, associativity, identity and invertibility), taking the identity n-braid to be n straight strands (i.e., a braid with no crossings). The braid generators also satisfy two (and only two) additional fundamental relations, namely, $\sigma_i\sigma_j = \sigma_j\sigma_i$ if $|i-j| \geq 2$ and $\sigma_i\sigma_{i+1}\sigma_i = \sigma_{i+1}\sigma_i\sigma_{i+1}$. All other relations can be derived from these two braid relations and the basic group operations.

Definition of the braid writhe and length. As discussed in the main text, the writhe (Wr) of a braid is a measure of the net amount of twisting and is defined as the sum of the exponents in the braid word. For example, considering the braid in Fig. S.1*c*, which is described by the braid word $\sigma_2\sigma_1^{-1}\sigma_2$, the writhe is computed as $\mathrm{Wr} = 1 - 1 + 1 = 1$. The length ($L$) of a braid, on the other hand, is a measure of the total amount of crossings and is defined as the absolute sum of the exponents in the braid word. Again, using the braid in Fig. S.1*c* as an example, the length is computed as $L = |1| + |-1| + |1| = 3$. The writhe is a braid invariant, meaning that so long as two braids are equivalent, regardless of their braid word, their writhes will be the same. Conversely, the length is not a braid invariant unless the braid is first reduced to its minimal representation, which is generally not a simple task. For instance, consider two braids, $\mathbf{a} = \sigma_1^{-1}\sigma_2\sigma_1\sigma_2\sigma_1^{-1}\sigma_2^{-1}$ and $\mathbf{b} = \sigma_1\sigma_2\sigma_2\sigma_1^{-1}\sigma_2^{-1}\sigma_1^{-1}\sigma_1^{-1}\sigma_2$, both of which are in fact equivalent to the identity. The writhe of both braids is 0, just like the identity braid, however their lengths are respectively 6 and 8 (i.e., not invariant). Since the minimal representation of each of these braids is the identity, their minimal length (L_c) is 0, which is an invariant.

Definition of the isotopy class specified by a braid. Every braid labels one of three types of isotopy classes given by the Thurston-Nielsen classification theorem: finite-order (or periodic), reducible or pseudo-Anosov. A braid ($\mathbf{b}$) is finite-order if through repeated application ($\mathbf{b}^m$, for some $m > 0$) we either recover the identity or a braid that can be 'undone' if we include rotations of its boundaries (i.e., with the endpoints being fixed relative to each other). A braid is reducible if it can be 'reduced' to a simpler braid by grouping strands that interact only amongst themselves; the braids within these groups are ultimately either finite-order or pseudo-Anosov. Finally, a braid is pseudo-Anosov if it is neither finite-order nor reducible. Following Smith and Warrier (2016), Fig. S.3 shows examples of these three classes of braids. Figure S.3*a* shows two finite-order braids, the 'full-twist' braid ($\sigma_1\sigma_2\sigma_1\sigma_2\sigma_1\sigma_2$) and another braid ($\sigma_1^{-1}\sigma_2\sigma_1\sigma_2\sigma_1^{-1}\sigma_2^{-1}$) that is equivalent to the identity. Note that the full-twist braid can be undone by rotating

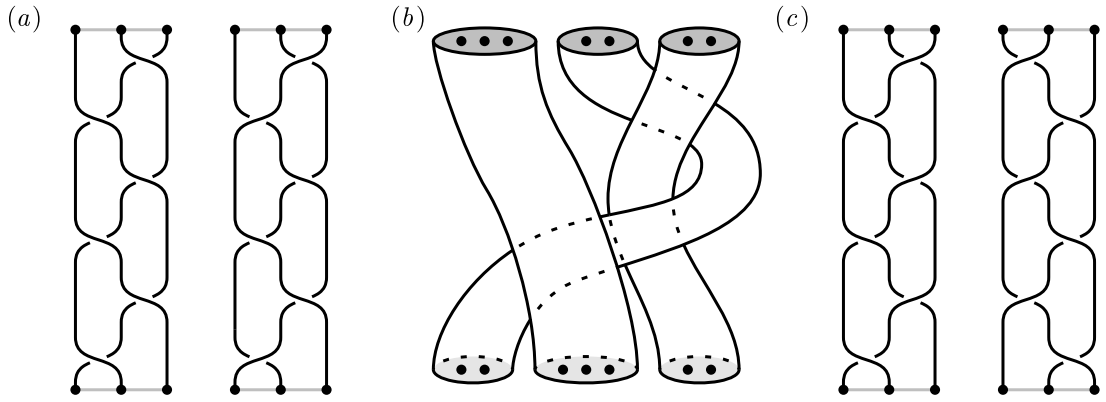

Figure S.3: (*a*) Two finite-order braids. The first is known as the 'full-twist' braid ($\sigma_1\sigma_2\sigma_1\sigma_2\sigma_1\sigma_2$) and the other is equivalent to the identity ($\sigma_1^{-1}\sigma_2\sigma_1\sigma_2\sigma_1^{-1}\sigma_2^{-1}$). If the grey line at the upper boundary of the full-twist braid is rotated counterclockwise a single time as viewed from above (with the strands 'glued' to the line), the braid reduces to the identity. (*b*) A reducible 7-braid where within each of the 3 tubes (or ropes) lies either a finite-order or pseudo-Anosov braid (one with 3 strands and two with 2 strands). (*c*) Two pseudo-Anosov braids: the 'golden' braid ($\sigma_1\sigma_2^{-1}$) and its inverse ($\sigma_2\sigma_1^{-1}$), both shown repeated three times.

the upper boundary counterclockwise, as viewed from above, through one full rotation (as though the endpoints were embedded onto the grey line in the figure). Figure S.3*b* depicts a reducible braid, where the 7 strands can be subdivided into 3 self-interacting subbraids, consisting of 3 separate ropes that are braided together. Figure S.3*c* depicts two pseudo-Anosov braids, the 'golden' braid ($\sigma_1\sigma_2^{-1}$) and its inverse ($\sigma_2\sigma_1^{-1}$). For further reading, refer to Birman (1975).

B. Topological representation of material stretching using loops

Translation of closed material curves to loops. The application of braid theory to fluid flows is particularly useful when we consider the interaction of particle trajectories on closed material curves or loops. Just as braids are used as the topological representation of particle trajectories and record crossing information, loops are used as the topological representation of closed material curves and record stretching information. Any material line in a flow acts as a barrier to fluid transport (by advection), in other words, the surrounding particle trajectories can deform and stretch a material line but never cross it (except, of course, by diffusion). Therefore, examining how the length of a material line grows in time as it is stretched and distorted by the surrounding particle trajectories can inform us on the degree of mixing occurring in the flow. Let us therefore begin from the same example as in Fig. 7 of the main text, reproduced here as Fig. S.4 for convenience. Consider the particle trajectories in Fig. S.4*a* with a material loop surrounding the blue (b) and white (w) particles. An additional small point is included in the loop, called the base point, which does not participate in the braid. Figure S.4*b* shows the particles projected on a horizontal line below the domain ($\alpha = 0$). As the particles undergo their clockwise and counterclockwise interchanges, the loop is stretched due to it being snagged on the particles; think of the loop as a taut rubber band. In this case, the loop in Fig. S.4*b* is acted on by the braid $\sigma_2\sigma_1^{-1}\sigma_2$ (i.e., that in Fig. S.1*c*).

Representation of loops in Dynnikov coordinates. Evidently, computing the actual length of the loop in Fig. S.4*a* or S.4*b* is not quite practical, especially when considering many particles or long advection times. Rather than computing the actual length of the loop, it suffices to use a simpler quantity that grows at the same exponential rate, namely, the number of intersections of the loop with a horizontal line to the left of the base point; this is what we will refer to as the 'length' of the loop. A convenient way of approaching this problem is by expressing the loop in what are known as Dynnikov coordinates. The reason for this approach is that given an initial loop (l), the Dynnikov coordinates of the loop ($\mathbf{l}_\mathcal{D}$) as well as the length of the loop can be easily updated according to the action

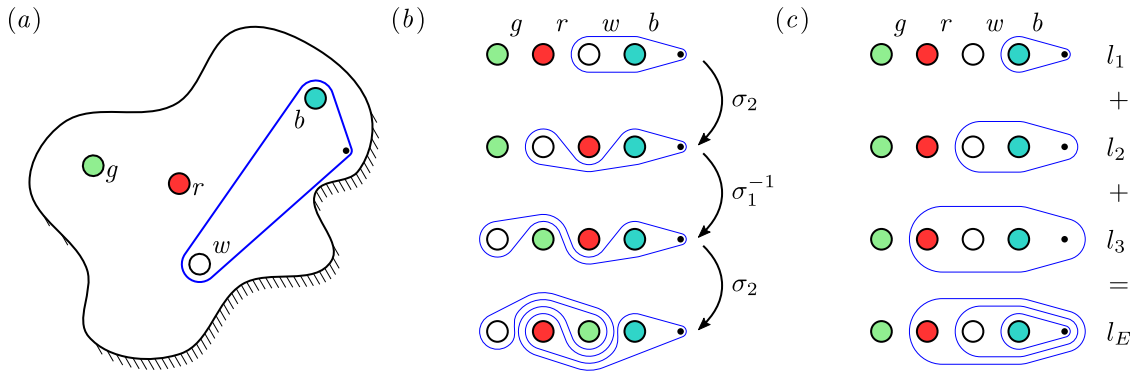

Figure S.4: (a) Example loop surrounding three particles, the smallest of which is a base point that does not participate in the braid formed in Fig. S.1. (b) The deformation of the loop, in a topological sense, under the action of the braid of Fig. S.1, namely, $\sigma_2\sigma_1^{-1}\sigma_2$. ($c$) The set of loops ($l_E$) considered in the finite-time braiding exponent in Eq. (S.3) consisting of consecutive loops that encircle the base point and each particle in succession (excluding the projected particle that is the furthest from the base point).

of a braid generator-by-generator using the set of update rules defined in Thiffeault (2010). To express the loop in Dynnikov coordinates, begin by drawing vertical lines between each pair of particles as well as vertical lines through particles 2 to $n-1$, as in Fig. S.5; here, $n=5$ including the base point. We then count the number of crossings of the loop above and below each particle, with the crossings above assigned the odd index of the variable μ_i and the crossings below the even index. The number of crossings between the particles is also counted, with ν_i representing the number of crossings between particle i and $i+1$. This indexing is also illustrated in Fig. S.5, where $\mu_{1,4}=2$, $\mu_{2,3}=0$, $\mu_{5,6}=1$ and $\nu_{1,2,3,4}=2$. Once μ_i and ν_i are known, we can express the loop in Dynnikov coordinates as

$$\mathbf{l}_{\mathcal{D}} = \begin{bmatrix} a_1 & \cdots & a_{n-2} & b_1 & \cdots & b_{n-2} \end{bmatrix}, \tag{S.1}$$

where

$$a_i = \frac{1}{2}\left(\mu_{2i} - \mu_{2i-1}\right) \quad \text{and} \quad b_i = \frac{1}{2}\left(\nu_i - \nu_{i+1}\right) \tag{S.2}$$

for $i = \{1, 2, ..., n-2\}$. The Dynnikov coordinate vector for the loop in Fig. S.5 is therefore $\begin{bmatrix} -1 & 1 & 0 & 0 & 0 & 0 \end{bmatrix}$. As mentioned in the main text, there can be bad choices of loops that will not be deformed by the braid, such as a loop surrounding the base point and the blue (b) particle in Fig. S.4*b*. Therefore, in order to guarantee that a braid deforms a selected loop, Budišić and Thiffeault (2015) suggested using the loop l_E depicted in Fig. S.4*c*; this is the reason for including the base point in Fig. S.4. The Dynnikov coordinate vector for the loop l_E in Fig. S.4*c* is given by $\begin{bmatrix} 0 & 0 & 0 & -1 & -1 & -1 \end{bmatrix}$. This is the process by which the loop lengths ($|\cdot|$) in the finite-time braiding exponent (Budišić & Thiffeault, 2015), defined as

$$\mathrm{FTBE} = \frac{1}{T}\log\frac{|\mathbf{b}l_E|}{|l_E|}, \tag{S.3}$$

are evaluated in `braidlab` (Thiffeault & Budišić, 2013–2019); T being the time interval of interest and $\mathbf{b}$ the braid formed by the particle trajectories. The FTBE provides an estimation of the topological entropy of the flow, namely, the maximum asymptotic growth rate of material lines (Newhouse & Pignataro, 1993; Thiffeault, 2010). The topological entropy is a global measure of loss of information about particle trajectories and therefore also a good measure of mixing quality.

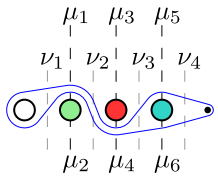

Figure S.5: Determination of the intersection numbers μ_i and ν_i for an example loop to be expressed in Dynnikov coordinates. For this loop, $\mu_{1,4}=2$, $\mu_{2,3}=0$, $\mu_{5,6}=1$ and $\nu_{1,2,3,4}=2$. The Dynnikov coordinate vector for the loop is $\begin{bmatrix} -1 & 1 & 0 & 0 & 0 & 0 \end{bmatrix}$.

II. Convergence of the braid properties

Cardiovascular flows pose several particular challenges that must be overcome in order to benefit from the braid approach. Specifically, cardiovascular flows are generally open systems and so particles will inevitably flee the region of interest at some point in time. The isolated left ventricle, for example, is an open system with blood flowing in from the mitral valve and out from the aortic valve. Moreover, the typical healthy left ventricle is able to eject at least 55% of its volume per beat, about half of which is 'old' blood (Bolger et al., 2007; Eriksson et al., 2013; Hendabadi et al., 2013; Di Labbio et al., 2018). In other words, blood that has entered the left ventricle in a given beat will be nearly completely cleared 2-3 beats later. Since longer trajectories (i.e., longer advection/tracking times) are generally required for the convergence of the properties of a braid (Budišić & Thiffeault, 2015; Filippi et al.,

2020), it may be that convergence cannot be achieved for some cardiovascular flows due to the restrictive time frames that particle trajectories have to become sufficiently entangled (i.e., before they exit the flow geometry of interest). We therefore evaluated the braid properties only over a characteristic time frame in our study and recommend the same for future cardiovascular flow studies. For the atria and ventricles of the heart, their respective filling phases are particularly useful since no particles are lost until they begin their ejection phases. In other cardiovascular flows, where an outflow may always be present (e.g., aneurysms, vessels), it may instead be possible to consider a set of particles that remain within the region of interest for some characteristic duration, and so the system will be effectively closed as far as the advection of those particles is concerned. Nonetheless, in the most general scenario, one has to decide how to treat fleeing particles. The most natural choice is to make particles stop participating in the braid once they flee, in the sense that other particles can no longer become entangled with them.

Another particular challenge that may affect the convergence of the properties of a braid is the number of available or computed particle trajectories participating in the braid (n). The convergence of some properties, such as the finite-time braiding exponent (FTBE), as a function of the number of trajectories can be rather slow (Budišić & Thiffeault, 2015; Filippi et al., 2020). For similar reasons, Thiffeault (2010) suggested considering a 'spectrum of braid entropies' rather than relying on its convergence to the topological entropy. Given that the FTBE is a generalization of the braid entropy to aperiodic trajectories (Budišić & Thiffeault, 2015), this suggests reporting a set of n-particle braiding exponents (FTBE_n) for various n. Since the objective always remains to extract global mixing information from the constructed braids, we seeded our left ventricular flow models with n randomly distributed particles and computed the braid properties for different n. Again, we recommend the same for future cardiovascular flow studies. Lastly, for a given n, one should ideally repeat the calculations using different random configurations of particles, and therefore test for convergence in the mean (and statistics) of the braid properties over a number of samples (2 000 in our case).

In the main text, we report the mean braid properties and other statistics by considering 2 000 different samples of 50 randomly selected particle trajectories advected over the diastolic duration (i.e., from $t^* = 0$ to t^*_{d}). In this section, we discuss the convergence of the braid properties in more detail by examining how they vary in time (over the diastolic duration) as well as with respect to the number of samples (up to 2 000) and the number of advected particles (10 to 400). Due to the similarity of the convergence behaviour observed between all the left ventricular flow models considered in the main text, we restrict our discussion to that of the healthy left ventricle model and provide the corresponding figures for the remaining cases in the appendix of this supplementary document.

A. The normalized braid writhe

Variation of the normalized writhe with time. Let us begin by examining the convergence behaviour of the braid writhe (Wr) in time. In the main text, we normalize the writhe by the square of the number of participating particle trajectories (i.e., we use Wr/n^2) and so we proceed in the same fashion here. We offer a technical note regarding alternative normalizations at the end of this subsection. Figure S.6*a* shows how the mean normalized writhe for 50 particles varies in time from the start to the end of the diastolic duration. A lightly coloured band marks one standard deviation above and below the mean. We have computed 2 000 samples of random braids to evaluate these statistics where, at any given time τ^* in Fig. S.6*a*, only the portion of the braids from $t^* = 0$ to τ^* are used. The mean normalized writhe and its standard deviation can both be seen to grow with time, though at a rate that is modulated by the flow dynamics, specifically by the strength of the cardiac vortex in this case. Being dependent on the number of crossings in a braid, the writhe of a braid is not a property that is expected to converge in time since longer trajectories will generally result in longer braids (i.e., more total crossings). Nevertheless, the existence of a preferred direction of rotation in the flow will cause the writhe to either increase (clockwise rotation) or decrease (counterclockwise rotation) in time. In the case of the healthy left ventricular flow, in Fig. S.6*a*, we can observe that the mean normalized writhe is increasing due to the clockwise swirling motion that persists throughout the diastolic duration. The rate of increase of the writhe, however, diminishes toward the end of the diastolic duration

due to a decay in vorticity of the cardiac vortex. This clear time-varying behaviour is why we suggest to use a fixed characteristic duration of a cardiovascular flow when reporting the braid properties.

Convergence of the normalized writhe according to the number of samples. In the main text, we report the braid properties at the end of the diastolic duration, in other words, the full braids formed by the trajectories over the entire advection period are considered. In Fig. S.6*b*, we therefore show how the mean and standard deviation, evaluated at the end of diastole, converge over the 2 000 samples (i). There is a clear convergence of the normalized writhe with respect to the number of samples. Furthermore, good results are achieved for both the mean and standard deviation rather quickly. For instance, an error of $\sim 5\%$ can be observed using only 10 or so samples while an error of $\sim 1\%$ can be observed using ~ 100 samples. There is therefore no need to obtain as many as 2 000 samples, as done in the main text.

Convergence of the normalized writhe according to the number of participating particle trajectories. Other than convergence with respect to the number of samples, the mean normalized writhe also converges with respect to the number of particles (n) participating in the braid, as illustrated in Fig. S.6*c*. To be more precise, for each n, we evaluate the mean and standard deviation of Wr/n^2 at the end of the diastolic duration and consider 2 000 samples. Indeed, using only 50 particles, as done throughout the main text, the mean normalized writhe has attained 98% of its converged value. Using fewer particles also yields good results with an error of 10% being observed for 10 particles and 4% for 25 particles. Moreover, the standard deviation of the normalized writhe is seen to decrease as more particles are considered. This is evidenced further in Fig. S.6*d* where the relative standard deviation (RSD) of the normalized writhe is shown to decrease with n; the relative standard deviation refers to the standard deviation divided by the mean. This suggests that, as more particles are considered, the convergence of the mean normalized writhe occurs more quickly (i.e., using fewer samples). For example, Fig. S.7 shows the variation of the 200-particle mean normalized writhe in time (Fig. S.7*a*) and with respect to the number of samples (Fig. S.7*b*) using the same limits and scales of the axes as in Fig. S.6. In time, the width of the standard deviation band is clearly shorter than that observed for 50 particles in Fig. S.6*a*. In terms of convergence with respect to the number of samples, Fig. S.7*b* shows smaller fluctuations of the mean normalized writhe early-on when compared to Fig. S.6*b*. In fact, $\sim 1\%$ error is achieved using 25 samples in this case.

Behaviour of the normalized writhe as a function of disease severity. While we do provide figures equivalent to that of Fig. S.6 in the appendix of this document for the diseased left ventricular flows discussed in the main text, we believe it is worth illustrating how the mean normalized writhe as a function of disease severity is affected by a change in the number of selected particles. Figure S.8*a* therefore shows the result using 10 particles and Fig. S.8*b* using 200 particles. For both subfigures, the same limits and scales of the axes in Fig. 5*a* of the main text (for 50 particles) are used to facilitate the comparison. It is remarkable to observe how insensitive the mean normalized writhe is to the number of particles being used, regardless of disease severity. Not only are the values similar between 10, 50 and 200 particles, but the overall trend with respect to the severity is very well preserved as the corresponding Pearson correlations with the circulation (Γ_{d}^{*}) remain the same ($r = 0.96$, $p = 0.003$). Therefore, highly representative results of the flow can be achieved using as few as 10 particles provided convergence is ensured with regard to the number of samples. Although not shown here, using 10 particles, an error of $\sim 10\%$ is achieved using 100 samples and $\sim 1\%$ using 500 samples. Considering what we observe for 50 and 200 particles above, we can suggest a rule of thumb, namely, that $\sim 1\%$ error in the mean normalized writhe can be achieved when the product of the number of participating particle trajectories (n) and the number of samples (i) is 5 000. Note, however, that this does not mean that we require 5 000 distinct particle trajectories since individual trajectories can be reused to generate different braid samples. One may, for instance, consider a combinatorial approach as discussed in Budišić and Thiffeault (2015).

Normalization of the writhe by the length of the braid. In the main text, we normalize the braid writhe (Wr) by the square of the number of particles (n) participating in the braid (i.e., Wr/n^2). This normalization is done, in part, to avoid reporting large values of the writhe. Particularly, given that the writhe is a braid invariant,

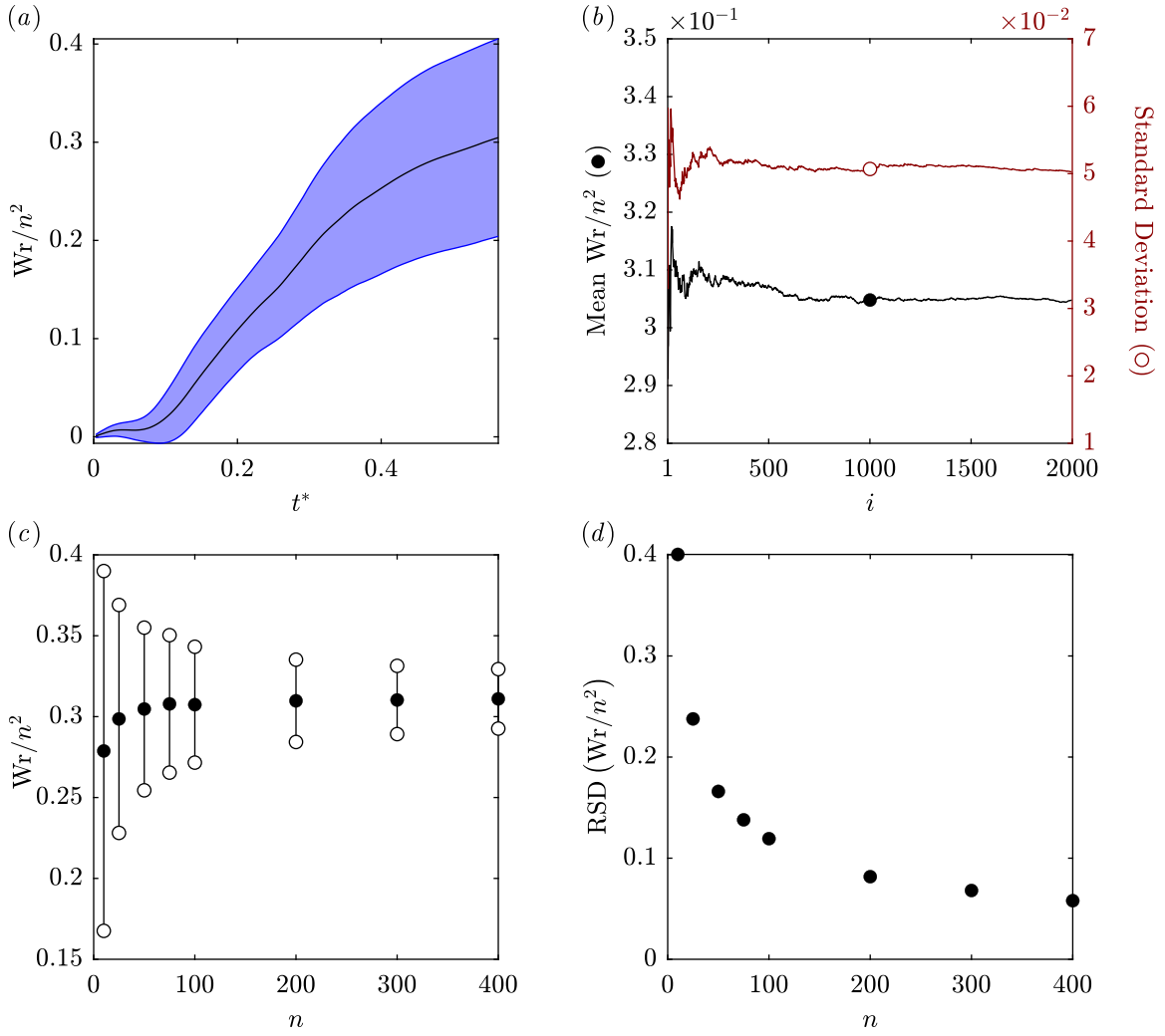

Figure S.6: (*a*) Variation of the mean normalized writhe (Wr/n^2) throughout the diastolic duration considering 50 particles and 2 000 samples. The lightly shaded band marks one standard deviation above and below the mean. (*b*) Variation of the mean (left axis, solid circle) and standard deviation (right axis, open circle) evaluated at the end of diastole over 2 000 samples (i). (*c*) Variation of the mean (solid circles) with respect to the number of particles (n) participating in the braid. For each n, the writhe is evaluated at the end of the diastolic duration and considers 2 000 samples. The open circles mark one standard deviation above and below the mean. (*d*) The corresponding relative standard deviation (RSD), namely, the standard deviation normalized by the mean.

using n^2 as the normalization factor retains this property. One may instead wish to normalize the writhe by the length (L) of the braid, in other words, by the total amount of crossings in the braid. Such a normalization would appear to be convenient and desirable as it produces a value of $+1$ if all the crossings in the braid are clockwise and -1 if all the crossings are counterclockwise. Unfortunately, the length of a braid is not a braid invariant. In other words, two equivalent braids can have very different lengths, however they will always possess the same writhe. This is rather easy to understand since we can always add the couple of generators $\sigma_i\sigma_i^{-1}$ to a braid (which is of course the identity), thus increasing its length by 2 without affecting the writhe. Note further that such an addition can be done *ad infinitum*. Evidently, this can pose a problem since two equivalent braids will not necessarily possess the same ratio Wr/L (although they will possess the same sign). Specifically, if we choose to use Wr/L rather than Wr/n^2, we run the risk of drawing incorrect conclusions since we can judge the preference in the direction of rotation

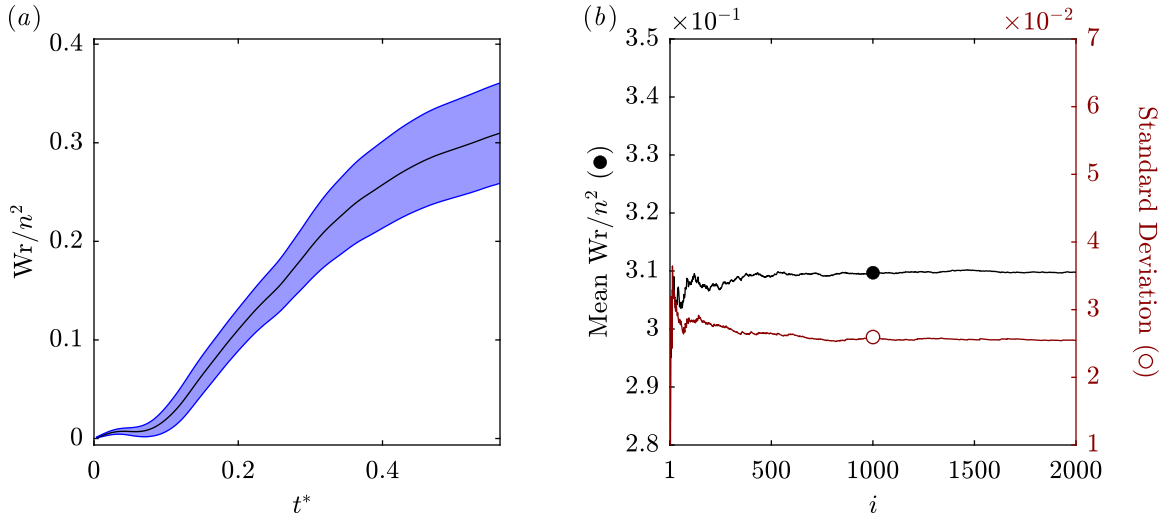

Figure S.7: (*a*) Variation of the mean normalized writhe (Wr/n^2) throughout the diastolic duration for 200 particles over 2 000 samples. The lightly shaded band marks one standard deviation above and below the mean. (*b*) Variation of the mean (left axis, solid circle) and standard deviation (right axis, open circle) evaluated at the end of diastole over 2 000 samples (i). For ease of comparison, for both subfigures, the same limits and scales of the axes are used as for 50 particles in Fig. S.6.

of one flow to be stronger or weaker than another when in fact they may be the same if the extracted braids were equivalent.

Normalization of the writhe by the minimal length of the braid. Nevertheless, there is a way that we can use the braid length to normalize the writhe and maintain its braid invariance; however, this requires additional work

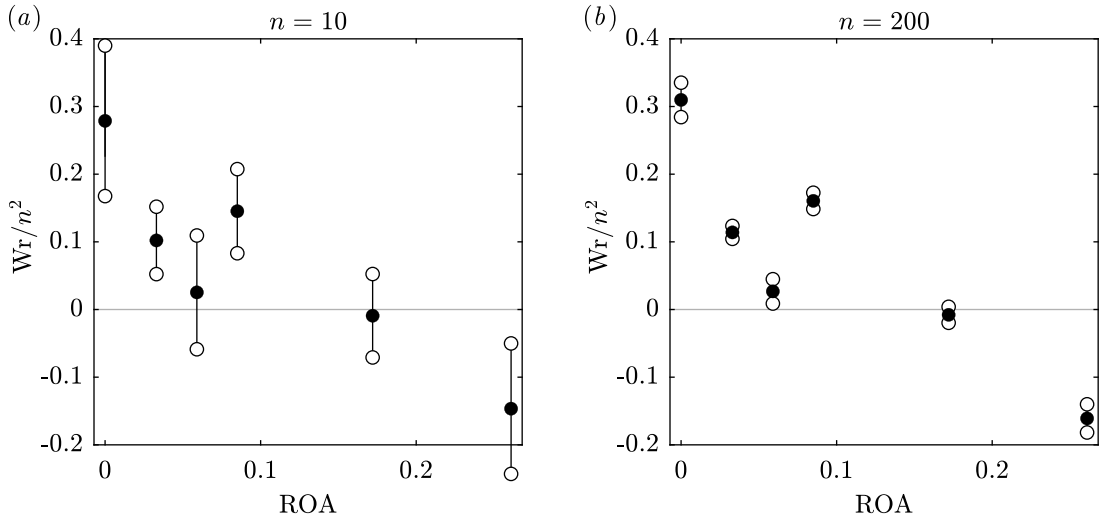

Figure S.8: (*a*) Variation of the mean normalized writhe (Wr/n^2) with the severity of the disease using 10 particles. (*b*) The corresponding variation using 200 particles. In each case, the writhe is evaluated at the end of the diastolic duration over 2 000 samples. The severity of the disease is here measured using the dimensionless regurgitant orifice area (ROA) as described in the main text and increases from left to right in the subfigures. For ease of comparison, for both subfigures, the same limits and scales of the axes are used as for 50 particles in Fig. 5*a* of the main text.

and is generally a difficult problem (Paterson & Razborov, 1991). Effectively, a braid can be 'simplified' through the use of the braid relations (and the basic group operations) in the sense that we can reduce its overall length without fundamentally changing it (i.e., the braid will still be equivalent to the original). It is therefore not hard to imagine that there must be a minimal length (L_c) of the braid that can be achieved after simplifying it as much as possible. This minimal length is a braid invariant. Therefore, if we normalize the writhe by this minimal length (i.e., Wr/L_c), we obtain a braid invariant property. Following the same conditions as for Fig. S.6, Fig. S.9 shows the convergence behaviour of this alternative form of normalized writhe (Wr/L_c) for the healthy left ventricle with respect to time (Fig. S.9*a*), the number of samples (Fig. S.9*b*) and the number of particles (Fig. S.9*c*, *d*). The results behave in very much the same way as the previous normalization (Wr/n^2) though it correlates slightly less with the circulation (Γ_d^*), showing a Pearson correlation coefficient of $r = 0.94$ ($p = 0.005$) compared to the previous result of

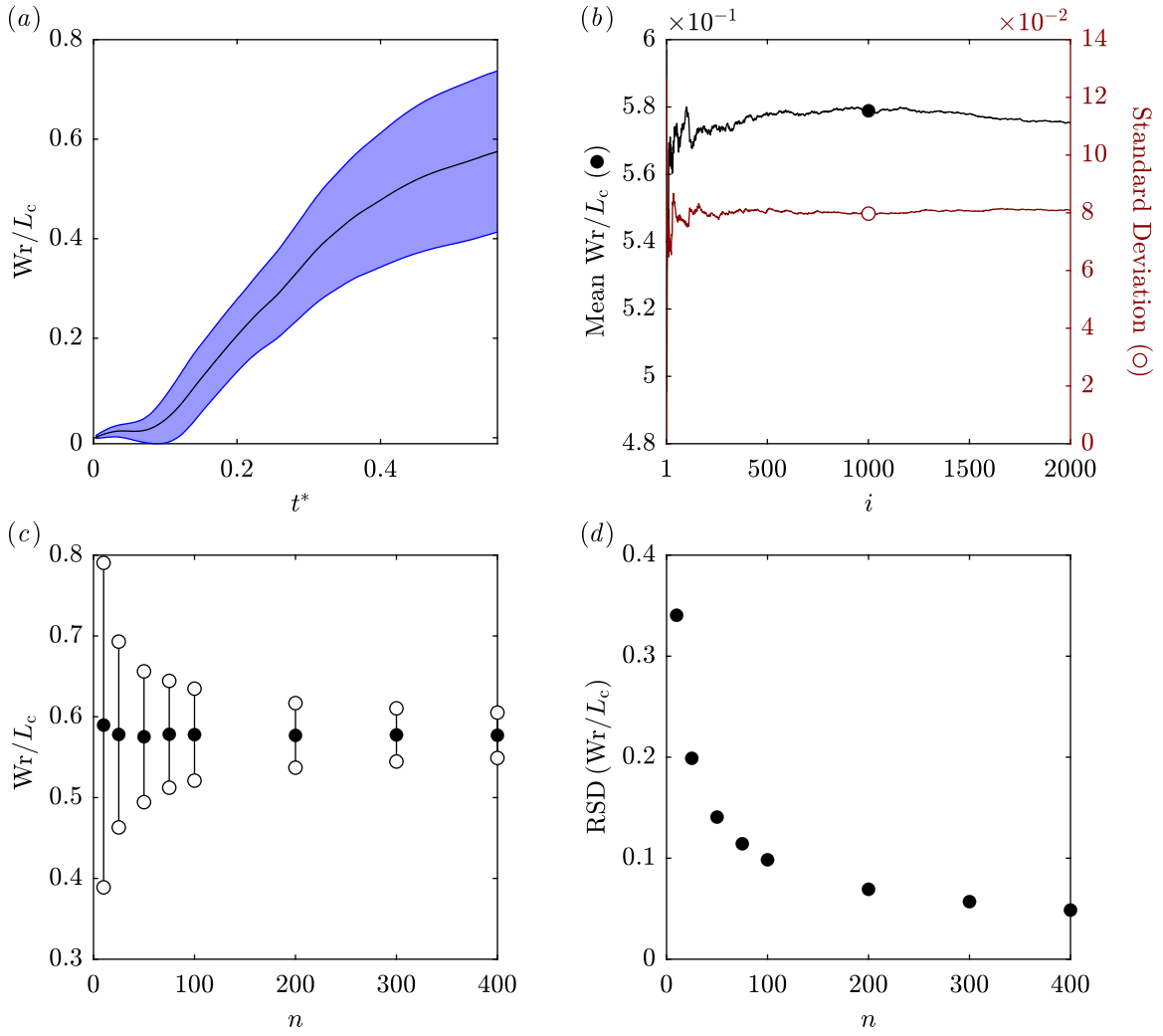

Figure S.9: (*a*) Variation of the alternative mean normalized writhe (Wr/L_c) throughout the diastolic duration for 50 particles over 2 000 samples. The lightly shaded band marks one standard deviation above and below the mean. (*b*) Variation of the mean (left axis, solid circle) and standard deviation (right axis, open circle) evaluated at the end of diastole over 2 000 samples (*i*). (*c*) Variation of the mean (solid circles) with respect to the number of particles (n) participating in the braid. For each n, the writhe is evaluated at the end of the diastolic duration and considers 2 000 samples. The open circles mark one standard deviation above and below the mean. (*d*) The corresponding relative standard deviation (RSD), namely, the standard deviation normalized by the mean.

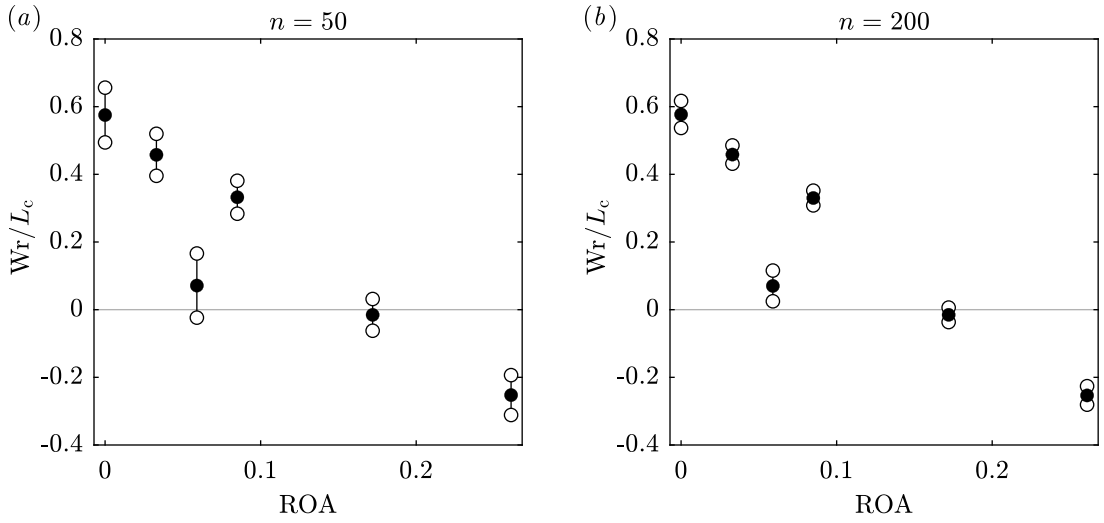

Figure S.10: (*a*) Variation of the alternative mean normalized writhe (Wr/L_c) with the severity of the disease using 50 particles. (*b*) The corresponding variation using 200 particles. In each case, the writhe is evaluated at the end of the diastolic duration over 2 000 samples. The severity of the disease is here measured using the dimensionless regurgitant orifice area (ROA) as described in the main text and increases from left to right in the subfigures.

$r = 0.96$ ($p = 0.003$). This slight decrease in correlation can be seen directly from the behaviour of this alternative mean normalized writhe as a function of disease severity in Fig. S.10. Note the increase in the value of the mild severity (ROA = 0.033) relative to the others. Such a difference between Wr/L_c and Wr/n^2 can occur because, in the former, the writhe and minimal length can grow at different and possibly competing rates while in the latter, the writhe is simply divided by a constant. In summary, we recommend using Wr/n^2 rather than Wr/L_c since this avoids the need for the calculation of the minimal length (i.e., a difficult co-NP-complete problem) and does not interfere with the actual behaviour of the writhe.

B. The fraction of pseudo-Anosov braids

In the main text, the fraction of pseudo-Anosov braids (f_pA) is evaluated by examining 2 000 samples of random braids and determining how many of them specify the pseudo-Anosov isotopy class. We are solely interested in the isotopy classes specified by the full braids, namely, considering the entire diastolic duration. Unlike the writhe and the finite-time braiding exponent, convergence in time of this quantity has little importance as it is effectively a Boolean variable and will either remain 0 (specifying the reducible or finite-order isotopy classes) or switch to 1 (specifying the pseudo-Anosov isotopy class) as the braid continues to form in time. Likewise, a standard deviation cannot be defined. We therefore only consider the convergence of the fraction of pseudo-Anosov braids in terms of the number of samples and the number of particles. Furthermore, we restrict our investigation to the use of 10, 25 and 50 particles as determining the isotopy class becomes prohibitively (exponentially) expensive as more particles are used.

Convergence of the fraction of pseudo-Anosov braids. Figure S.11 illustrates the convergence of the fraction of pseudo-Anosov braids as we consider more samples of random braids (up to 2 000). In Fig. S.11*a*, the result is shown for 10 and 25 particles while in Fig. S.11*b* it is shown for 50 particles. As observed for the mean normalized writhe, the convergence of the fraction of pseudo-Anosov braids improves as we consider more particles. For 10, 25 and 50 particles, the converged values respectively amount to 0.611, 0.831 and 0.842. Satisfactory results can therefore be achieved with only 25 particles for the healthy left ventricle. Using 10 samples, the respective errors

amount to $\sim 25\%$, $\sim 20\%$ and $\sim 10\%$ while for 100 samples, the respective errors reduce to $\sim 15\%$, $\sim 8\%$ and $\sim 2\%$. As for the mean normalized writhe, we can suggest a heuristic guideline, namely, that $\sim 2\%$ error in the fraction of pseudo-Anosov braids can be attained when the product of the number of participating particle trajectories (n) and the number of samples (i) is 5 000.

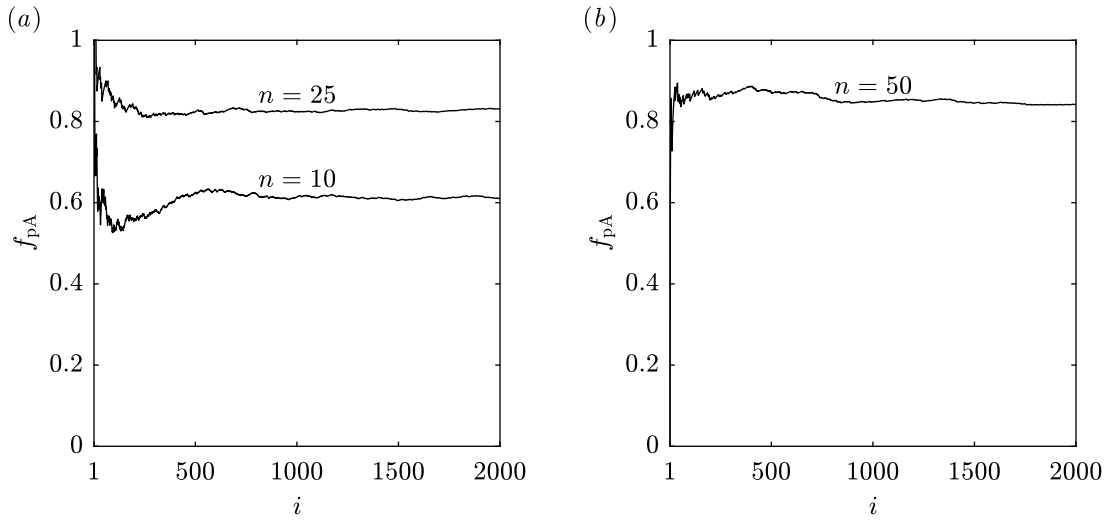

Figure S.11: (a) Convergence of the 10- and 25-particle fractions of pseudo-Anosov braids (f_{pA}) evaluated at the end of the diastolic duration over 2 000 samples of random braids (i). (b) Convergence of the 50-particle fraction of pseudo-Anosov braids.

Behaviour of the fraction of pseudo-Anosov braids as a function of disease severity. Let us now examine how the use of 10 and 25 particles affects the relationship between the fraction of pseudo-Anosov braids and the severity of the aortic regurgitation disease studied in the main text. This is illustrated in Fig. S.12a for 10 particles and Fig. S.12b using 25 particles. For both subfigures, the same limits and scales of the axes in Fig. 7a of the main text (for 50 particles) are used to simplify the comparison. While there is a noticeable change in the values of the fraction of pseudo-Anosov braids as we move from 10 to 25 particles, very little change is observed from 25 to 50. In any case, whether we consider 10, 25 or 50 particles, the same conclusions can be drawn from these plots. For instance, in all cases, the healthy left ventricle is marked by an exceptionally high fraction of pseudo-Anosov braids. Furthermore, the overall trend with respect to the severity is also rather well preserved. To compare, the Pearson correlations between the fraction of pseudo-Anosov braids and the energy dissipation index ($\mathrm{EDI_d}$) for 10, 25 and 50 particles are respectively $r = 0.83$ ($p = 0.04$), $r = 0.96$ ($p = 0.003$) and $r = 0.93$ ($p = 0.008$). Therefore, once again, highly representative results of the flow can be obtained using even fewer particles than what has been considered in the main text (i.e., 50).

Additional note on the fraction of pseudo-Anosov braids relevant to the considered datasets. It is interesting to observe that the fraction of pseudo-Anosov braids correlates better with the energy dissipation index when using 25 particles compared to when using 50 particles. In general, the correlation is expected to improve as we use more particles, just as we observe between the mean normalized writhe and the circulation. This occurs purely as a result of the relative magnitudes of the fraction of pseudo-Anosov braids between the healthy scenario (ROA = 0) and the second moderate severity of aortic regurgitation (ROA = 0.085). Specifically, for 10 and 25 particles, it is clear that the fraction of pseudo-Anosov braids for the healthy scenario is the largest among all cases, suggesting its flow topology to be the most effective at mixing. This is promising since the healthy left ventricular flow model also shows the most efficient energetic behaviour (i.e., the lowest energy dissipation index). However, for 50 particles, the second moderate severity actually shows a slightly higher f_{pA}. This turns out to be a direct consequence of the way the datasets were acquired in the original experiments (Di Labbio & Kadem, 2018; Di Labbio

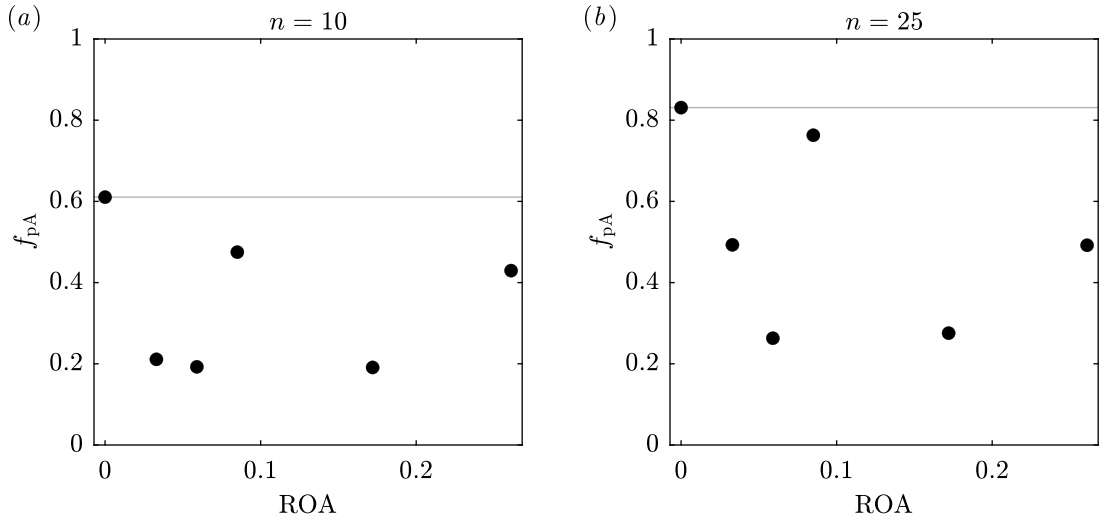

Figure S.12: (*a*) Variation of the fraction of pseudo-Anosov braids (f_{pA}) with the severity of the aortic regurgitation disease using 10 particles. (*b*) The corresponding variation using 25 particles. In each case, the fraction of pseudo-Anosov braids is evaluated at the end of the diastolic duration over 2 000 samples. The severity of the disease is here measured using the dimensionless regurgitant orifice area (ROA) as described in the main text and increases from left to right in the subfigures. For ease of comparison, for both subfigures, the same limits and scales of the axes are used as for 50 particles in Fig. 7*a* of the main text.

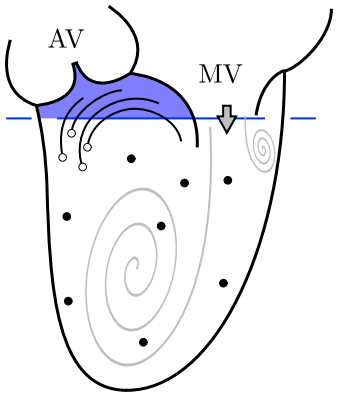

Figure S.13: Schematic of a dozen random particles in a healthy left ventricular flow. The horizontal line represents the boundary of the domain in the datasets of Di Labbio and Kadem (2019) and the shaded region is therefore not captured. Particles near the upper boundary (open circles) will flee early-on and produce reducible braids rather than pseudo-Anosov braids (if the full trajectories were captured).

et al., 2018). Due to the design of the left heart simulator, the measurement domain captured by the camera in the particle image velocimetry setup could not include a portion of the left ventricle model in the vicinity of the outflow tract. By consequence, some particles flee the domain during the diastolic duration even though they are not actually ejected from the left ventricle model. For the purposes of illustration, Fig. S.13 shows a schematic of a dozen random particles in the healthy left ventricle model. The horizontal line marks the boundary of the domain and the shaded region is therefore not captured. Randomly selected particles near the upper boundary of the domain on the side of the aortic valve (marked by open circles in Fig. S.13) will flee early-on and produce straight strands in the resulting braid. This in fact has the tendency to produce reducible braids since these strands will not become entangled with others. Indeed, if the shaded region in Fig. S.13 were captured, the particle trajectories would have participated in

the braid for a longer time and instead produce a pseudo-Anosov braid. Therefore, the loss of this region has the consequence of diminishing the fraction of observed pseudo-Anosov braids in the case of the healthy left ventricular flow model. This effect is also further exacerbated with the use of more particles since it will simply be more likely to select such particles (hence the better performance when using 25 particles rather than 50). In the presence of aortic regurgitation on the other hand, the absence of this region does not pose any problem as the regurgitant jet actually pushes these particles toward the centre of the left ventricle model in the early stages of diastole, thus allowing them to interact with other randomly selected particles within the flow.

C. The finite-time braiding exponent

Convergence of the finite-time braiding exponent with time. We examine the convergence behaviour of the finite-time braiding exponent (FTBE) in the same manner as the normalized writhe. Figure S.14*a* shows how the mean finite-time braiding exponent for 50 particles varies in time over the diastolic duration. As before, a lightly coloured band marks one standard deviation above and below the mean and, at each instant in time, the mean and standard deviation are computed over 2 000 samples. Contrary to the normalized writhe, the mean finite-time braiding exponent and its standard deviation are both observed to decay with time and appear to be converging, therefore suggesting the use of the diastolic duration to be rather appropriate. This suggests that a shorter advection time can in fact be tolerated and yield similar results (this is also true for the cases with aortic regurgitation).

Convergence of the finite-time braiding exponent according to the number of samples. The convergence of the mean and standard deviation, evaluated at the end of diastole, with respect to the number of samples (i) is shown in Fig. S.14*b*. Like the normalized writhe, convergence with respect to the number of samples occurs quite quickly. Using 10 samples, the mean already exhibits an error of only $\sim 3\%$ of its converged value. For 50 samples, the error falls to $\sim 1\%$ and for 100 samples to $\sim 0.5\%$. Therefore, far fewer than 2 000 samples are required to achieve satisfactory results.

Convergence of the finite-time braiding exponent according to the number of participating particle trajectories. Let us now consider the convergence of the mean finite-time braiding exponent with respect to the number of particles (n) participating in the braid. Figure S.14*c* depicts how the mean finite-time braiding exponent varies according to the number of randomly selected particles. As for the normalized writhe, for each n, we evaluate the mean and standard deviation at the end of the diastolic duration and consider 2 000 samples. As discussed in Budišić and Thiffeault (2015) and Filippi et al. (2020), convergence of the finite-time braiding exponent can be rather slow and this can be observed directly from Fig. S.14*c*. It is unclear if the mean FTBE is truly approaching an asymptotic value with n, however the overall trend is encouraging. The mean FTBE_n increases monotonically from 4.01 for 10 particles to 11.44 for 400 particles; however, the standard deviation actually decreases monotonically from 0.65 to 0.23 (relative standard deviation from 16.1% to 2.2%, refer to Fig. S.14*d*). In fact, a logarithmic function of the form $\text{FTBE} = 2.0533 \ln(n) - 1.0122$ provides a rather suitable fit ($r^2 = 0.9957$). For example, this logarithmic fit predicts a mean FTBE of 13.17 for 1 000 particles while the true value is actually found to be 13.44. Of course, a logarithmic trend suggests that the FTBE cannot converge, however a rational fit may also be possible. Indeed, it would be quite extraordinary if the healthy left ventricle could be characterized by a universal diastolic topological entropy (i.e., the limit of the FTBE with n). However, given the slow convergence, we further emphasize our recommendation in the main text to report a spectrum of values (FTBE_n) when possible, as Thiffeault (2010) first suggested for the braid entropy. Nonetheless, with more particles, the convergence of the FTBE does improve both with respect to time and the number of samples. Figure S.15 demonstrates this by plotting the variation of the 200-particle FTBE in time (Fig. S.15*a*) and with respect to the number of samples (Fig. S.15*b*). It is striking to observe how much the convergence has improved in both contexts. In fact, less than 1% error is achieved using 10 samples. In keeping with the previous subsections, the convergence rule of thumb here is therefore that $\sim 1\%$ error in the mean FTBE_n can be achieved when the product of the number of participating particle trajectories (n) and the number of samples (i) is 2 000.

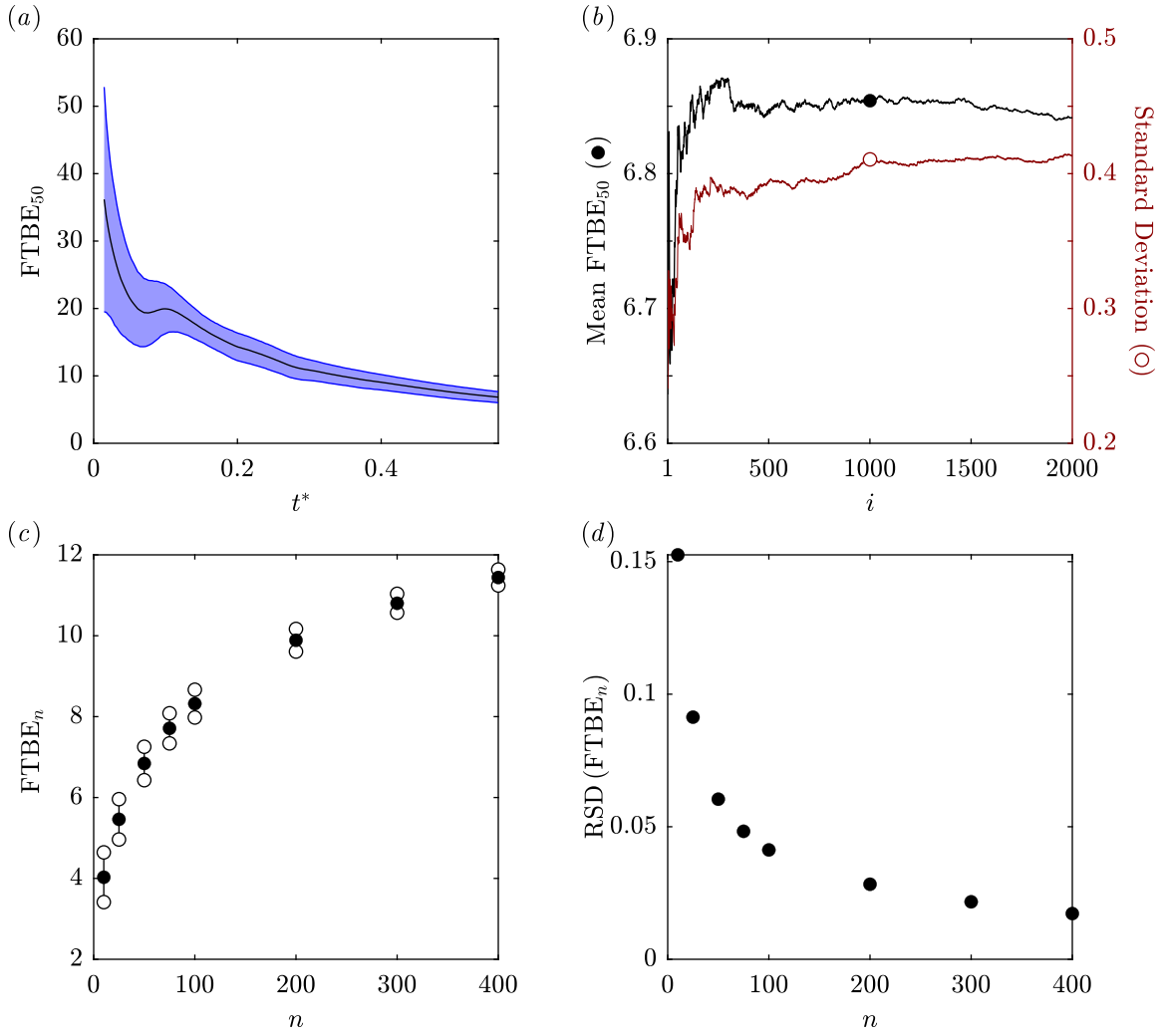

Figure S.14: (*a*) Variation of the mean finite-time braiding exponent (FTBE) throughout the diastolic duration considering 50 particles over 2 000 samples. The lightly shaded band marks one standard deviation above and below the mean. (*b*) Variation of the mean (left axis, solid circle) and standard deviation (right axis, open circle) evaluated at the end of diastole over 2 000 samples (*i*). (*c*) Variation of the mean (solid circles) with respect to the number of particles (n) participating in the braid. For each n, the finite-time braiding exponent is evaluated at the end of the diastolic duration and considers 2 000 samples. The open circles mark one standard deviation above and below the mean. (*d*) The corresponding relative standard deviation (RSD), namely, the standard deviation normalized by the mean.

Behaviour of the finite-time braiding exponent as a function of disease severity. Although the mean finite-time braiding exponent increases as we consider more particles, the variation of the mean as a function of the severity of the disease remains relatively unchanged regardless of how many particles are considered. Figure S.16*a* shows the mean 10-particle FTBE and Fig. S.16*b* the mean 200-particle FTBE. Whether considering 10 or 200 particles, as we progress from the healthy left ventricular flow model to the most severe case of aortic regurgitation (i.e., from left to right in Fig. S.16) the same behaviour is observed. The corresponding Pearson correlations with the mean finite-time Lyapunov exponent computed over diastole ($\mathrm{FTLE_d}$) for 10, 50 and 200 particles are respectively $r = 0.88$ ($p = 0.02$), $r = 0.93$ ($p = 0.007$) and $r = 0.92$ ($p = 0.009$). The slight decrease in the correlation as we move from 50 particles to 200 particles is again due to the loss of particles in the healthy left ventricular flow model, as

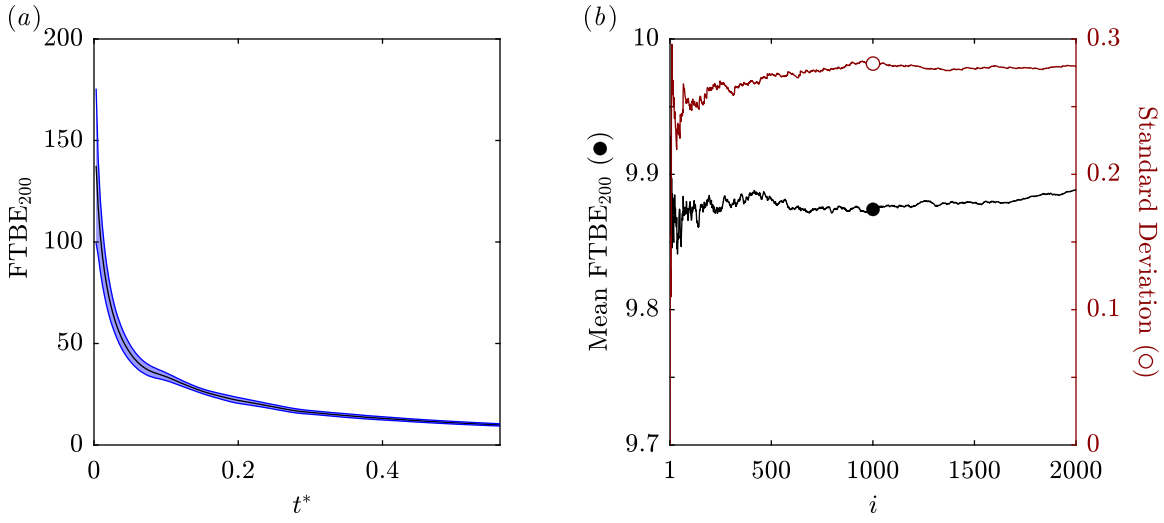

Figure S.15: (*a*) Variation of the mean finite-time braiding exponent (FTBE) throughout the diastolic duration for 200 particles over 2 000 samples. The lightly shaded band marks one standard deviation above and below the mean. (*b*) Variation of the mean (left axis, solid circle) and standard deviation (right axis, open circle) evaluated at the end of diastole over 2 000 samples (*i*). For ease of comparison, for the latter subfigure, the same scales of the axes (with different limits) are used as for 50 particles in Fig. S.14*b*.

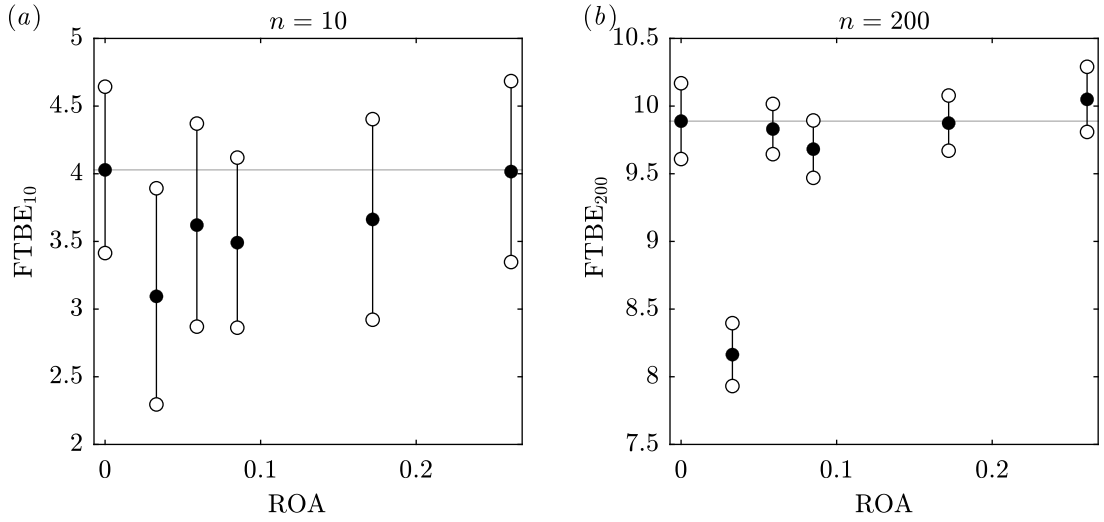

Figure S.16: (*a*) Variation of the mean finite-time braiding exponent (FTBE) with the severity of the disease using 10 particles. (*b*) The corresponding variation using 200 particles. In each case, the FTBE is evaluated at the end of the diastolic duration over 2 000 samples. The severity of the disease is here measured using the dimensionless regurgitant orifice area (ROA) as described in the main text and increases from left to right in the subfigures.

discussed in the previous subsection for the fraction of pseudo-Anosov braids. Nonetheless, once again, using as few as 10 randomly distributed particles, the same conclusions can be drawn from the converged mean FTBE.

III. Definitions of non-braid parameters

A. The circulation

The measure of circulation (Γ_{d}^{*}) used to produce Fig. 5*b* in the main text is defined by

$$\Gamma_{\mathrm{d}}^{*} = -\int_{t_{\mathrm{d}}} \frac{\Gamma(t)}{A(t)} \mathrm{d}t, \tag{S.4}$$

where $\Gamma(t)$ denotes the dimensional circulation computed within the entire left ventricle at any given time (t), $A(t)$ the area of the left ventricle (which changes with time) and t_{d} the diastolic duration. The measure given by Eq. (S.4) is a dimensionless quantity representing the integral of the circulation per unit area over the diastolic duration. The negative sign in Eq. (S.4) is added to emphasize the convention used in the main text, where a positive circulation represents a clockwise tendency of rotation as observed in the case of the healthy left ventricle. The circulation in Eq. (S.4) at any given time is computed from the spatial integral of the vorticity within the left ventricle, i.e.,

$$\Gamma(t) = \iint_{A(t)} \left(\frac{\partial v}{\partial x} - \frac{\partial u}{\partial y} \right) \mathrm{d}A, \tag{S.5}$$

where $u(x, y, t)$ and $v(x, y, t)$ denote the velocity components (at a given time) in the x and y directions respectively (i.e., a Cartesian coordinate system is being used).

B. The energy dissipation index

The measure of the energy dissipation index ($\mathrm{EDI}_{\mathrm{d}}$) used to produce Fig. 7*b* in the main text is defined by

$$\mathrm{EDI}_{\mathrm{d}} = \frac{t_{\mathrm{d}} \mathrm{VEL}_{\mathrm{d}}}{\mathrm{TKE}_{\mathrm{d}}}, \tag{S.6}$$

where t_{d} denotes the diastolic duration, $\mathrm{VEL}_{\mathrm{d}}$ the total viscous energy loss throughout diastole and KE_{d} the total flow kinetic energy contained within diastole. The measure given by Eq. (S.6) is a dimensionless quantity representing the ratio of viscous dissipation to flow kinetic energy as defined by Agati et al. (2014), though in our case the quantity is restricted to the diastolic duration. It essentially provides information on the ability of a flow to preserve its kinetic energy, where lower values indicate a better preservation. The total viscous energy loss is computed as

$$\mathrm{VEL}_{\mathrm{d}} = \int_{t_{\mathrm{d}}} \left(\iint_{A(t)} \frac{\mu}{2} \sum_{\forall i,j} \left(\frac{\partial u_i}{\partial x_j} + \frac{\partial u_j}{\partial x_i} \right)^2 \mathrm{d}A \right) \mathrm{d}t, \tag{S.7}$$

where $u_i(x_j, t)$ denotes the velocity components ($u_1 = u$, $u_2 = v$) at a given time (t) in the x_i direction ($x_1 = x$, $x_2 = y$; it is a Cartesian coordinate system), $\mu = 4.2$ cP the dynamic viscosity (Di Labbio & Kadem, 2018) and $A(t)$ the area of the left ventricle (which changes with time). The total flow kinetic energy is computed as

$$\mathrm{TKE}_{\mathrm{d}} = \int_{t_{\mathrm{d}}} \left(\iint_{A(t)} \frac{\rho}{2} \left(u^2 + v^2 \right) \mathrm{d}A \right) \mathrm{d}t, \tag{S.8}$$

where $u(x, y, t)$ and $v(x, y, t)$ denote the velocity components (at a given time) in the x and y directions respectively and $\rho = 1100$ kg/m^3 the density (Di Labbio & Kadem, 2018).

C. The finite-time Lyapunov exponent

The measure of the finite-time Lyapunov exponent ($\mathrm{FTLE_d}$) used to produce Fig. 9*b* in the main text is defined by

$$\mathrm{FTLE_d} = \int_{t_\mathrm{d}} \left(\frac{1}{A\,(t)} \iint_{A(t)} \mathrm{FTLE}\,(x,y,t)\,\mathrm{d}A \right) \mathrm{d}t, \tag{S.9}$$

where $\mathrm{FTLE}\,(x,y,t)$ denotes the finite-time Lyapunov exponent field at time instant t, $A\,(t)$ the area of the left ventricle (which changes with time) and t_d the diastolic duration. The measure given by Eq. (S.9) is a dimensionless quantity representing the integral of the spatial mean finite-time Lyapunov exponent over the diastolic duration. The finite-time Lyapunov exponent (FTLE) itself was computed in forward time only, following precisely the same procedure as discussed in Di Labbio et al. (2018), namely, including an 8-fold refinement of the grid and an integration (or advection) time of two cardiac cycles. Given that the datasets of Di Labbio and Kadem (2019) span one cardiac cycle, the data was simply appended to itself to consider more cycles. Furthermore, since we have used the reduced-order models generated from the dynamic mode decompositions (which reproduces periodicity very well), this concatenation is actually smooth (or seamless) in time.

References

Agati, L., Cimino, S., Tonti, G., Cicogna, F., Petronilli, V., De Luca, L., ... Pedrizzetti, G. (2014). Quantitative analysis of intraventricular blood flow dynamics by echocardiographic particle image velocimetry in patients with acute myocardial infarction at different stages of left ventricular dysfunction. *European Heart Journal – Cardiovascular Imaging*, **15**(11), 1203–1212.

Allshouse, M. R., & Thiffeault, J.-L. (2012). Detecting coherent structures using braids. *Physica D*, **241**(2), 95–105.

Artin, E. (1947). Theory of braids. *Annals of Mathematics*, **48**(1), 101–126.

Birman, J. S. (1975). *Braids, Links, and Mapping Class Groups*. Princeton, NJ: Princeton University Press.

Bolger, A. F., Heiberg, E., Karlsson, M., Wigström, L., Engvall, J., Sigfridsson, A., ... Wranne, B. (2007). Transit of blood flow through the human left ventricle mapped by cardiovascular magnetic resonance. *Journal of Cardiovascular Magnetic Resonance*, **9**(5), 741–747.

Budišić, M., & Thiffeault, J.-L. (2015). Finite-time braiding exponents. *Chaos*, **25**(8), 087407.

Di Labbio, G., & Kadem, L. (2018). Jet collisions and vortex reversal in the human left ventricle. *Journal of Biomechanics*, **78**, 155–160.

Di Labbio, G., & Kadem, L. (2019). Reduced-order modeling of left ventricular flow subject to aortic valve regurgitation. *Physics of Fluids*, **31**(3), 031901.

Di Labbio, G., Vétel, J., & Kadem, L. (2018). Material transport in the left ventricle with aortic valve regurgitation. *Physical Review Fluids*, **3**(11), 113101.

Eriksson, J., Bolger, A. F., Ebbers, T., & Carlhäll, C.-J. (2013). Four-dimensional blood flow-specific markers of LV dysfunction in dilated cardiomyopathy. *European Heart Journal – Cardiovascular Imaging*, **14**(5), 417–424.

Filippi, M., Budišić, M., Allshouse, M. R., Atis, S., Thiffeault, J.-L., & Peacock, T. (2020). Using braids to quantify interface growth and coherence in a rotor-oscillator flow. *Physical Review Fluids*, **5**(5), 054504.

Francois, N., Xia, H., Punzmann, H., Faber, B., & Shats, M. (2016). Braid entropy of two-dimensional turbulence. *Nature: Scientific Reports*, **5**(1), 18564.

Hendabadi, S., Bermejo, J., Benito, Y., Yotti, R., Fernández-Avilés, F., del Álamo, J. C., & Shadden, S. C. (2013). Topology of blood transport in the human left ventricle by novel processing of Doppler echocardiography. *Annals of Biomedical Engineering*, **41**(12), 2603–2616.

Newhouse, S., & Pignataro, T. (1993). On the estimation of topological entropy. *Journal of Statistical Physics*, **72**(5–6), 1331–1351.

Paterson, M. S., & Razborov, A. A. (1991). The set of minimal braids is co-NP-complete. *Journal of Algorithms*, **12**(3), 393–408.

Smith, S. A., & Warrier, S. (2016). Reynolds number effects on mixing due to topological chaos. *Chaos*, **26**(3), 033106.

Thiffeault, J.-L. (2005). Measuring topological chaos. *Physical Review Letters*, **94**(8), 084502.

Thiffeault, J.-L. (2010). Braids of entangled particle trajectories. *Chaos*, **20**(1), 017516.

Thiffeault, J.-L., & Budišić, M. (2013–2019). Braidlab: A software package for braids and loops. *arXiv: 1410.0849*, [**math.GT**], Version 3.2.4.

Thiffeault, J.-L., & Finn, M. D. (2006). Topology, braids and mixing in fluids. *Philosophical Transactions of the Royal Society of London A*, **364**(1849), 3251–3266.

Appendix

A. Convergence of braid properties for cases with aortic regurgitation

A. Mild aortic regurgitation (0.033 ROA)

1. The normalized braid writhe (0.033 ROA)

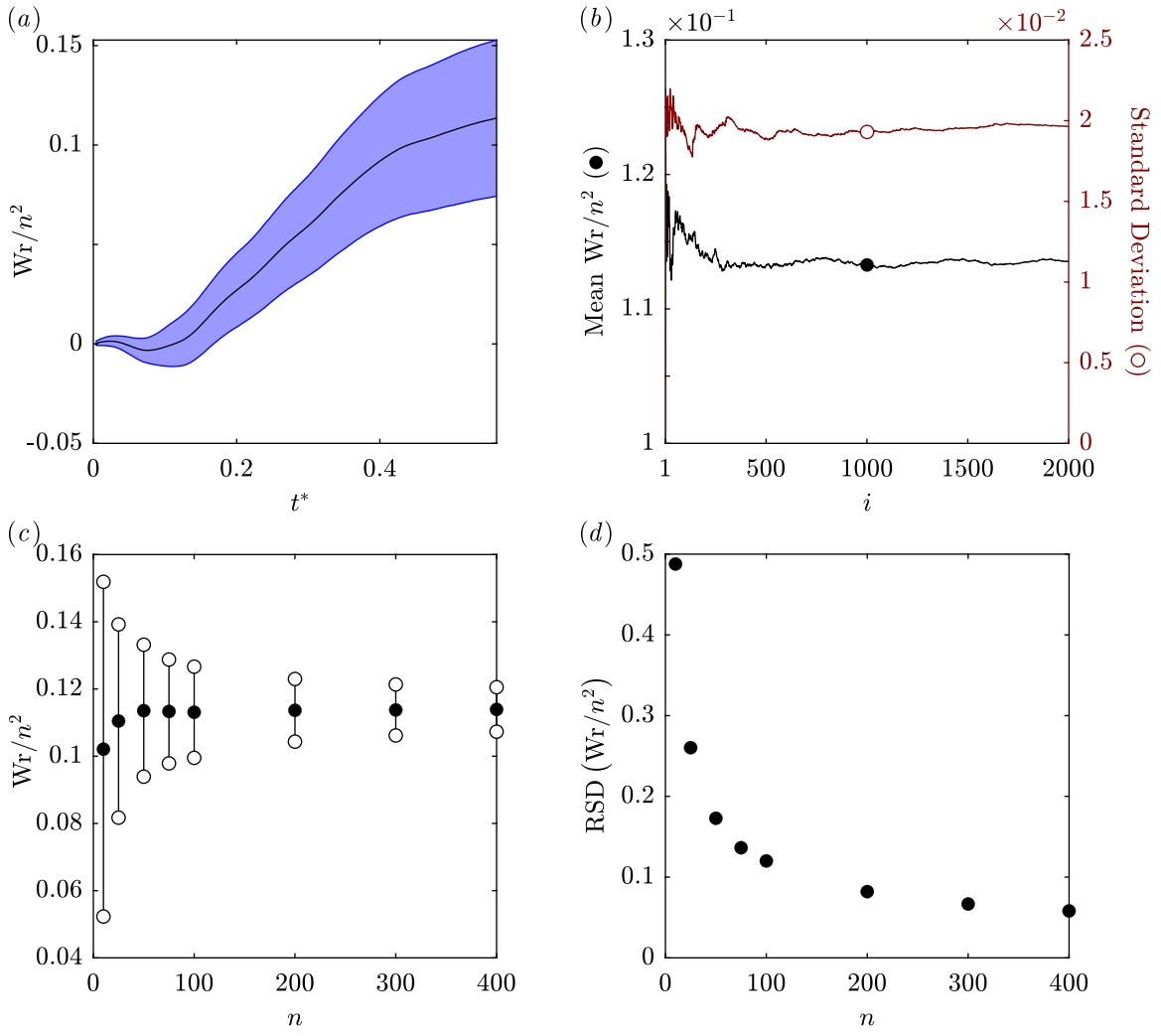

Figure S.A1: (a) Variation of the mean normalized writhe (Wr/n^2) throughout the diastolic duration for 50 particles over 2 000 samples. The lightly shaded band marks one standard deviation above and below the mean. (b) Variation of the mean (left axis, solid circle) and standard deviation (right axis, open circle) evaluated at the end of diastole over 2 000 samples (i). (c) Variation of the mean (solid circles) with respect to the number of particles (n) participating in the braid. For each n, the writhe is evaluated at the end of the diastolic duration and considers 2 000 samples. The open circles mark one standard deviation above and below the mean. (d) The corresponding relative standard deviation (RSD), namely, the standard deviation normalized by the mean.

2. The fraction of pseudo-Anosov braids (0.033 ROA)

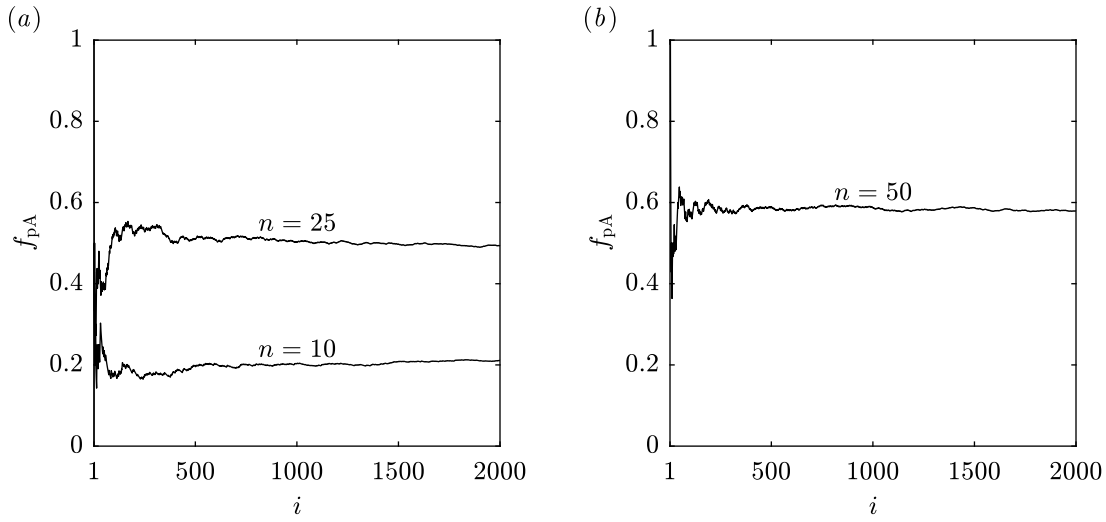

Figure S.A2: (a) Convergence of the 10- and 25-particle fractions of pseudo-Anosov braids (f_{pA}) evaluated at the end of the diastolic duration over 2 000 samples of random braids (i). (b) Convergence of the 50-particle fraction of pseudo-Anosov braids.

3. The finite-time braiding exponent (0.033 ROA)

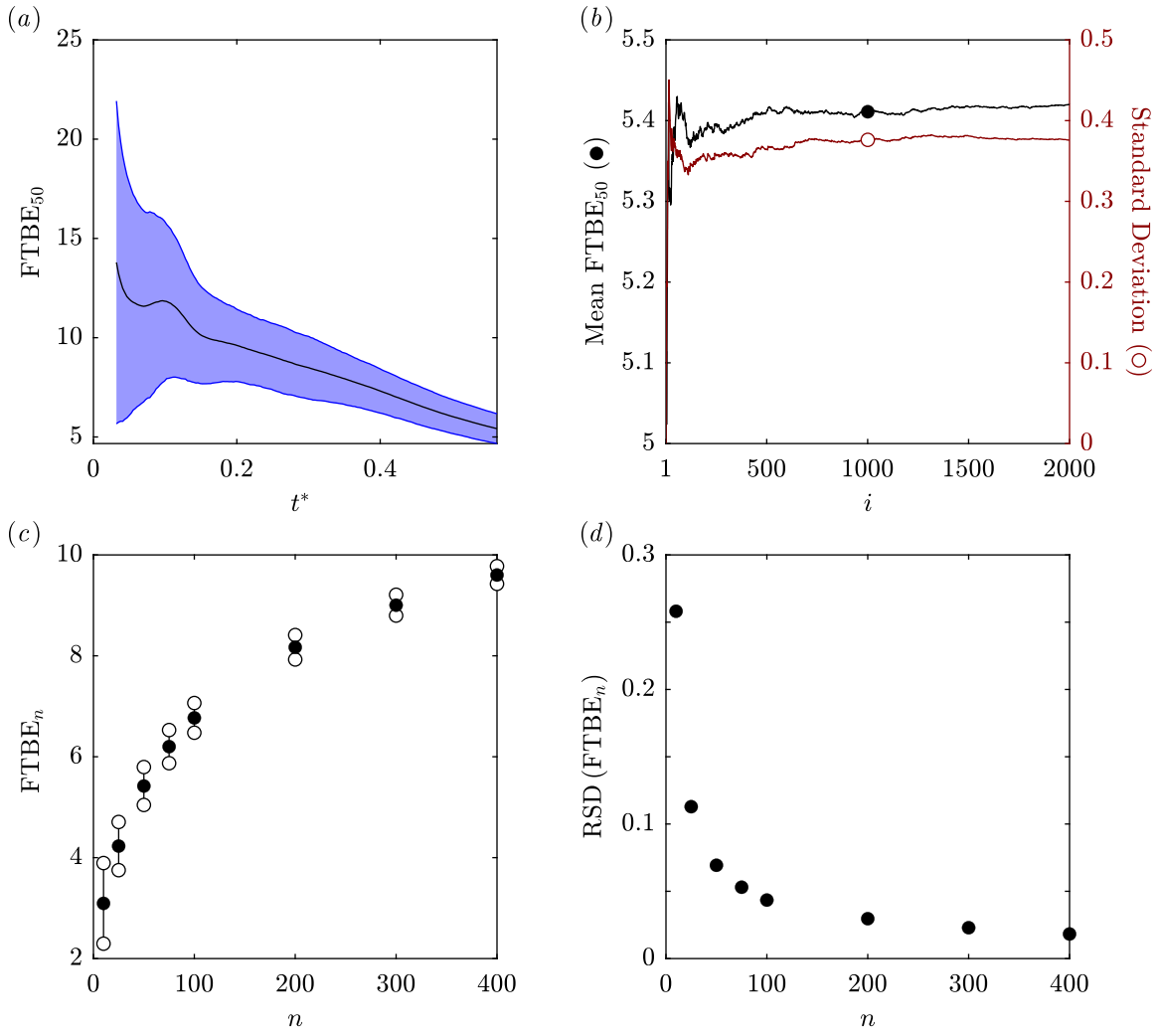

Figure S.A3: (*a*) Variation of the mean finite-time braiding exponent (FTBE) throughout the diastolic duration considering 50 particles over 2 000 sample. The lightly shaded band marks one standard deviation above and below the mean. (*b*) Variation of the mean (left axis, solid circle) and standard deviation (right axis, open circle) evaluated at the end of diastole over 2 000 samples (i). (*c*) Variation of the mean (solid circles) with respect to the number of particles (n) participating in the braid. For each n, the finite-time braiding exponent is evaluated at the end of the diastolic duration and considers 2 000 samples. The open circles mark one standard deviation above and below the mean. (*d*) The corresponding relative standard deviation (RSD), namely, the standard deviation normalized by the mean.

B. Moderate aortic regurgitation 1 (0.059 ROA)

1. The normalized braid writhe (0.059 ROA)

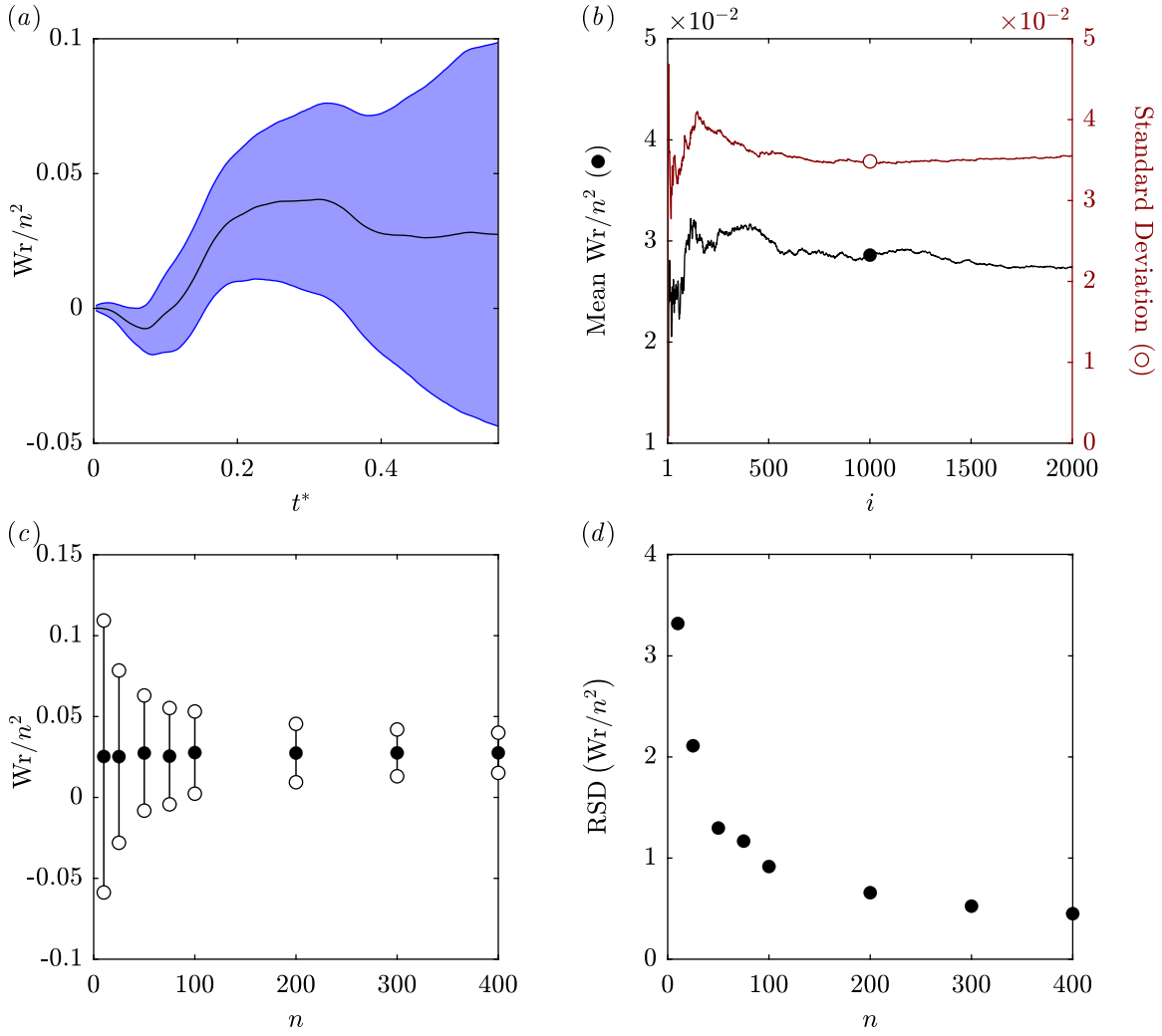

Figure S.A4: (a) Variation of the mean normalized writhe (Wr/n^2) throughout the diastolic duration for 50 particles over 2 000 samples. The lightly shaded band marks one standard deviation above and below the mean. (b) Variation of the mean (left axis, solid circle) and standard deviation (right axis, open circle) evaluated at the end of diastole over 2 000 samples (i). (c) Variation of the mean (solid circles) with respect to the number of particles (n) participating in the braid. For each n, the writhe is evaluated at the end of the diastolic duration and considers 2 000 samples. The open circles mark one standard deviation above and below the mean. (d) The corresponding relative standard deviation (RSD), namely, the standard deviation normalized by the mean.

2. The fraction of pseudo-Anosov braids (0.059 ROA)

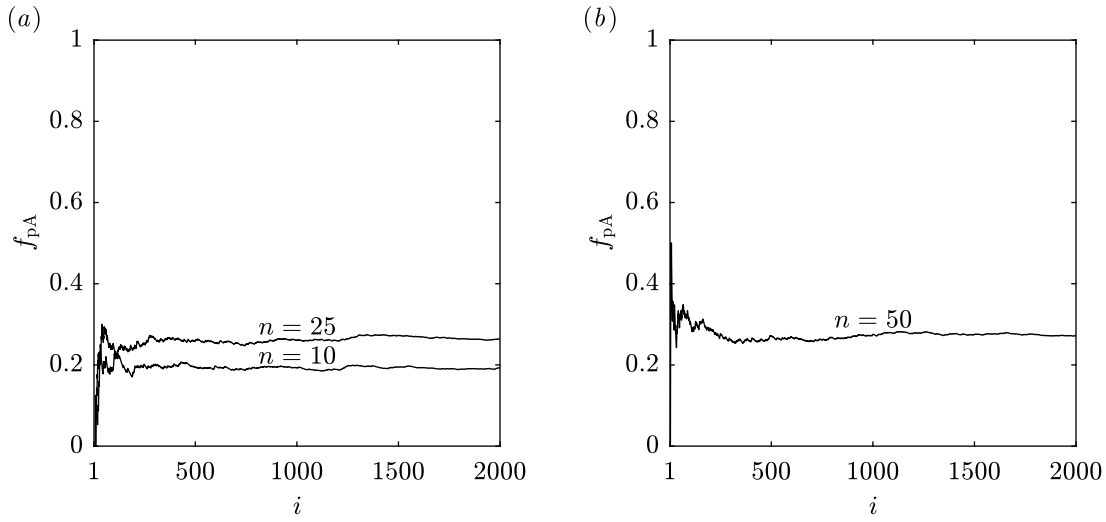

Figure S.A5: (*a*) Convergence of the 10- and 25-particle fractions of pseudo-Anosov braids (f_{pA}) evaluated at the end of the diastolic duration over 2 000 samples of random braids (i). (*b*) Convergence of the 50-particle fraction of pseudo-Anosov braids.

3. The finite-time braiding exponent (0.059 ROA)

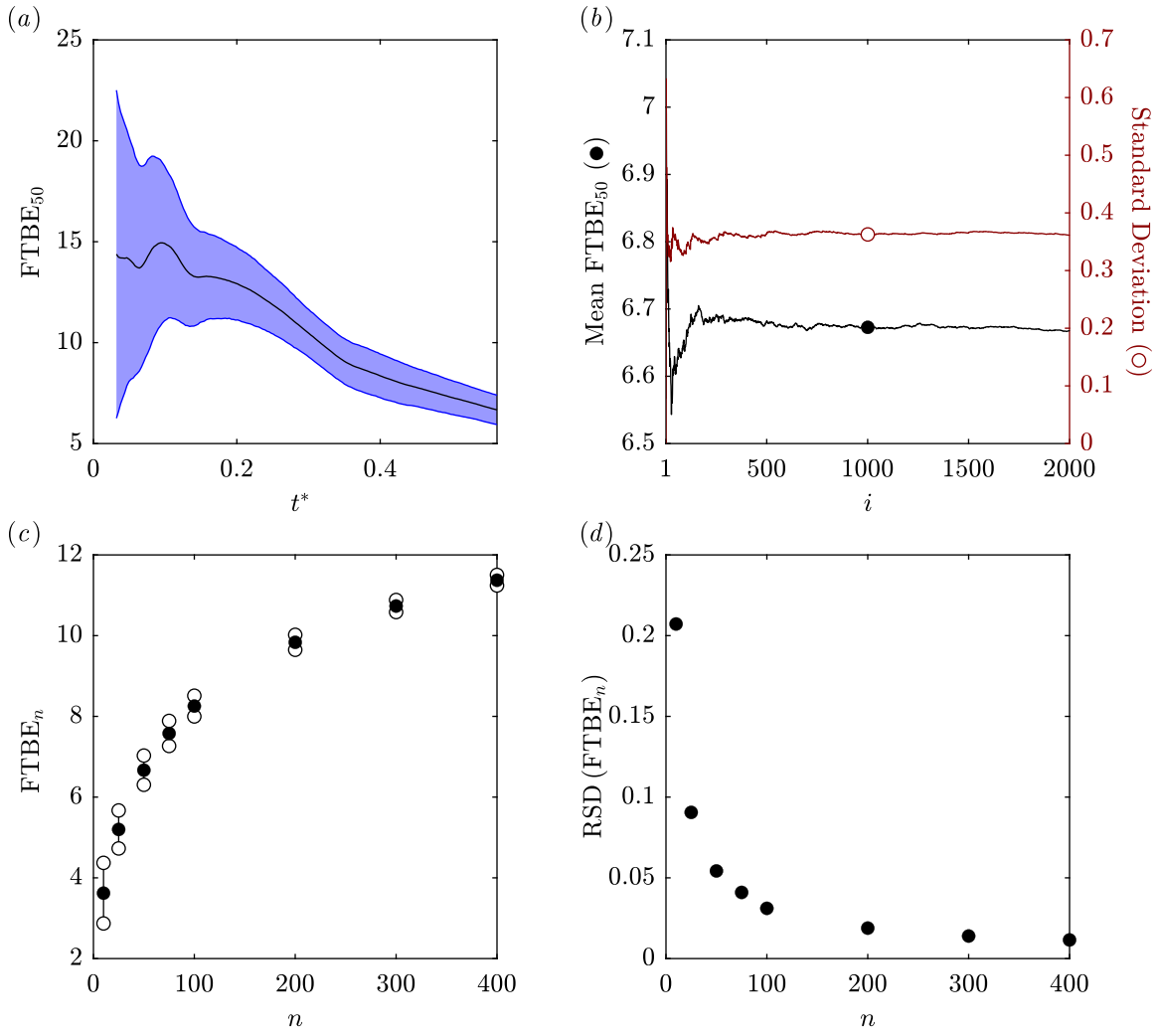

Figure S.A6: (*a*) Variation of the mean finite-time braiding exponent (FTBE) throughout the diastolic duration considering 50 particles over 2 000 sample. The lightly shaded band marks one standard deviation above and below the mean. (*b*) Variation of the mean (left axis, solid circle) and standard deviation (right axis, open circle) evaluated at the end of diastole over 2 000 samples (i). (*c*) Variation of the mean (solid circles) with respect to the number of particles (n) participating in the braid. For each n, the finite-time braiding exponent is evaluated at the end of the diastolic duration and considers 2 000 samples. The open circles mark one standard deviation above and below the mean. (*d*) The corresponding relative standard deviation (RSD), namely, the standard deviation normalized by the mean.

C. Moderate aortic regurgitation 2 (0.085 ROA)

1. The normalized braid writhe (0.085 ROA)

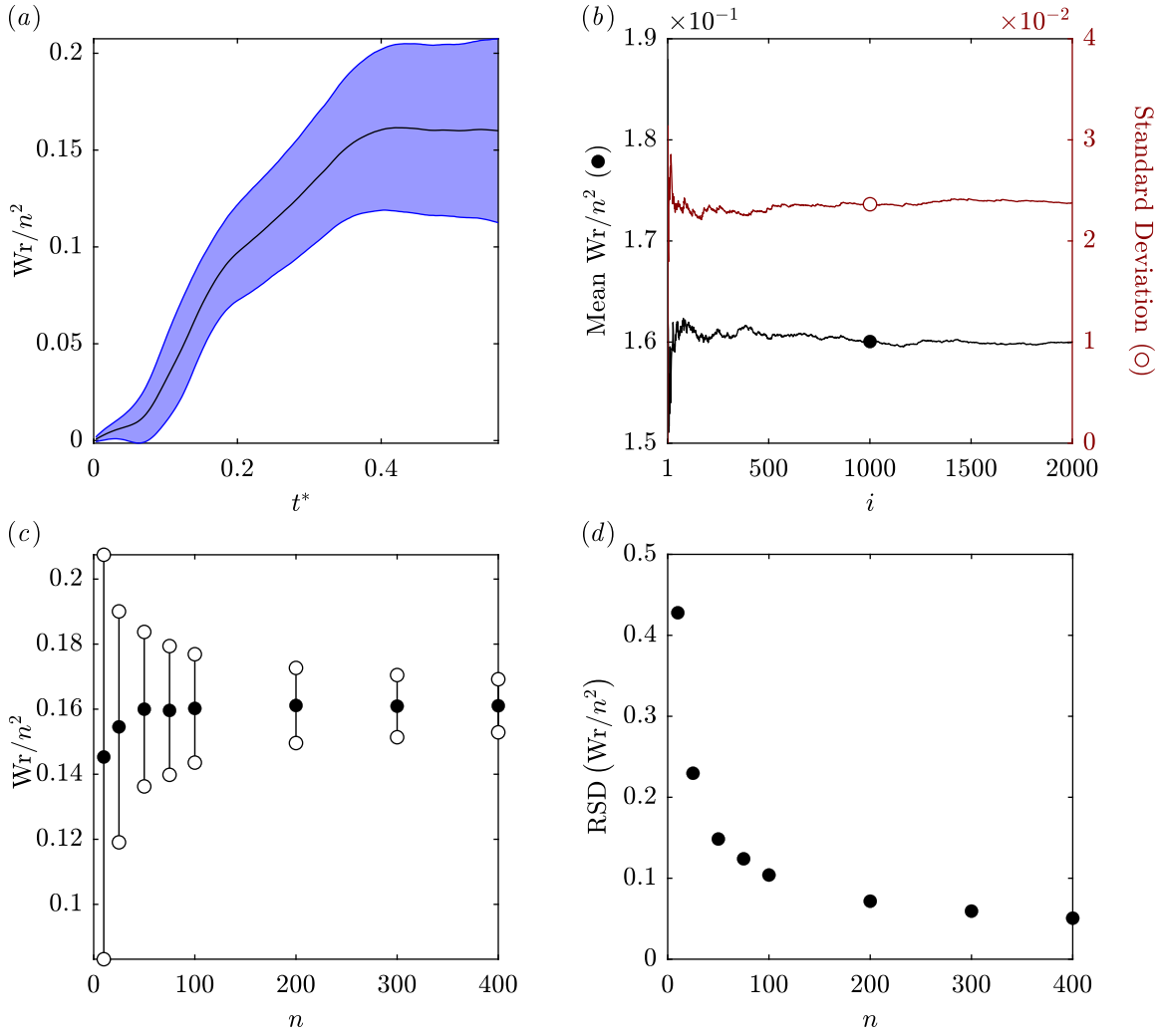

Figure S.A7: (a) Variation of the mean normalized writhe (Wr/n^2) throughout the diastolic duration for 50 particles over 2 000 samples. The lightly shaded band marks one standard deviation above and below the mean. (b) Variation of the mean (left axis, solid circle) and standard deviation (right axis, open circle) evaluated at the end of diastole over 2 000 samples (i). (c) Variation of the mean (solid circles) with respect to the number of particles (n) participating in the braid. For each n, the writhe is evaluated at the end of the diastolic duration and considers 2 000 samples. The open circles mark one standard deviation above and below the mean. (d) The corresponding relative standard deviation (RSD), namely, the standard deviation normalized by the mean.

2. The fraction of pseudo-Anosov braids (0.085 ROA)

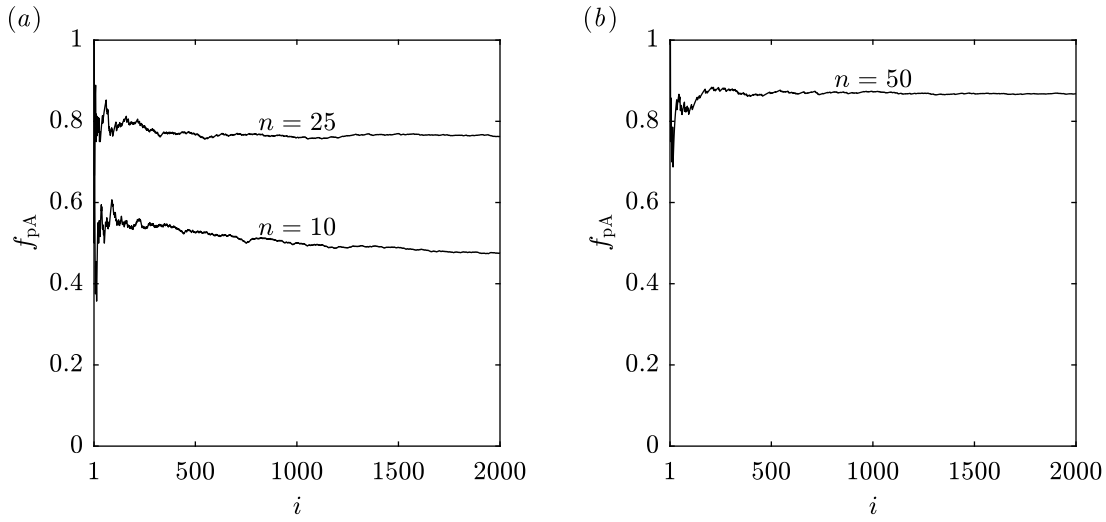

Figure S.A8: (*a*) Convergence of the 10- and 25-particle fractions of pseudo-Anosov braids (f_{pA}) evaluated at the end of the diastolic duration over 2 000 samples of random braids (i). (*b*) Convergence of the 50-particle fraction of pseudo-Anosov braids.

3. The finite-time braiding exponent (0.085 ROA)

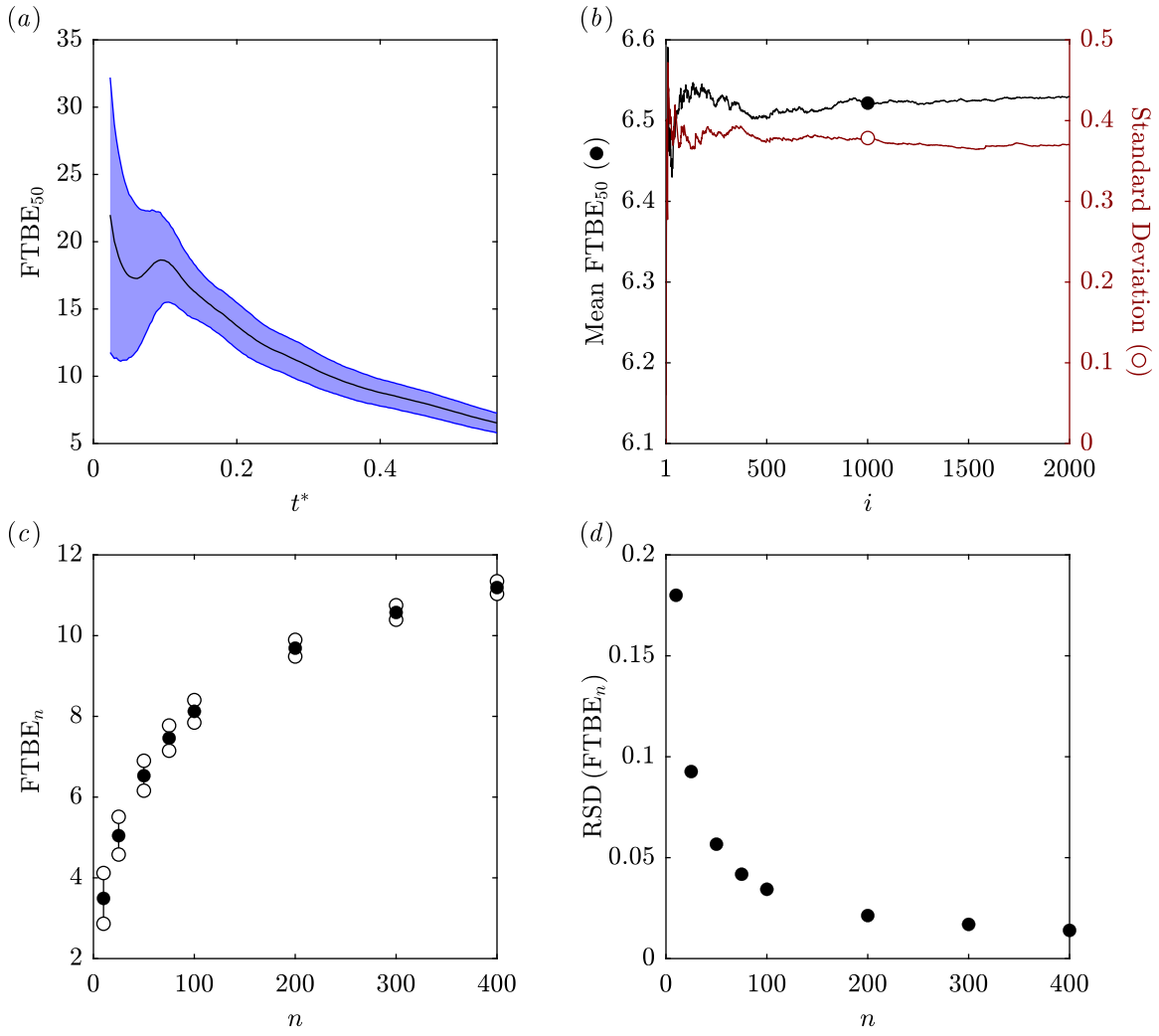

Figure S.A9: (*a*) Variation of the mean finite-time braiding exponent (FTBE) throughout the diastolic duration considering 50 particles over 2 000 sample. The lightly shaded band marks one standard deviation above and below the mean. (*b*) Variation of the mean (left axis, solid circle) and standard deviation (right axis, open circle) evaluated at the end of diastole over 2 000 samples (i). (*c*) Variation of the mean (solid circles) with respect to the number of particles (n) participating in the braid. For each n, the finite-time braiding exponent is evaluated at the end of the diastolic duration and considers 2 000 samples. The open circles mark one standard deviation above and below the mean. (*d*) The corresponding relative standard deviation (RSD), namely, the standard deviation normalized by the mean.

D. Severe aortic regurgitation 1 (0.172 ROA)

1. The normalized braid writhe (0.172 ROA)

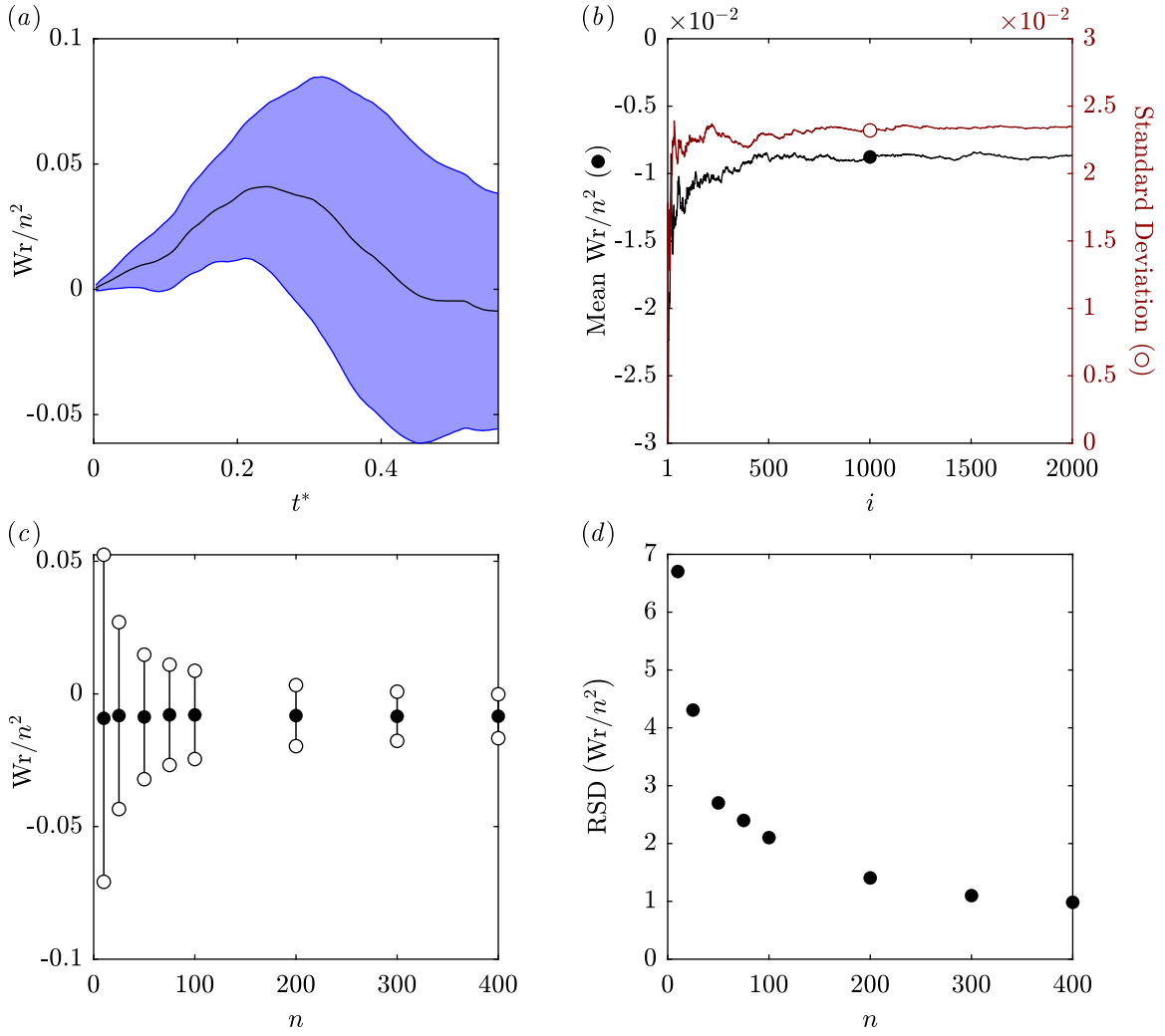

Figure S.A10: (*a*) Variation of the mean normalized writhe (Wr/n^2) throughout the diastolic duration for 50 particles over 2 000 samples. The lightly shaded band marks one standard deviation above and below the mean. (*b*) Variation of the mean (left axis, solid circle) and standard deviation (right axis, open circle) evaluated at the end of diastole over 2 000 samples (i). (*c*) Variation of the mean (solid circles) with respect to the number of particles (n) participating in the braid. For each n, the writhe is evaluated at the end of the diastolic duration and considers 2 000 samples. The open circles mark one standard deviation above and below the mean. (*d*) The corresponding relative standard deviation (RSD), namely, the standard deviation normalized by the mean.

2. The fraction of pseudo-Anosov braids (0.172 ROA)

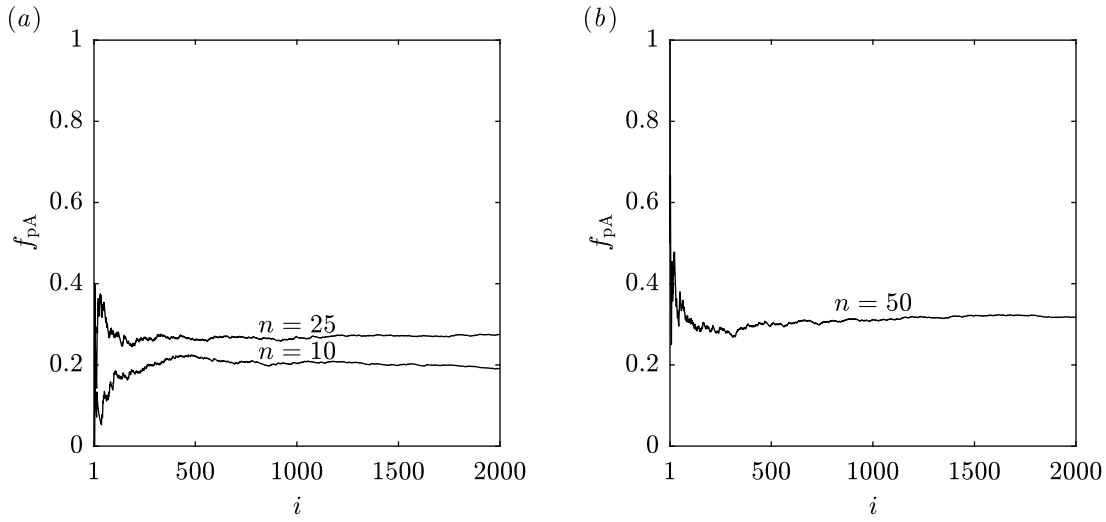

Figure S.A11: (*a*) Convergence of the 10- and 25-particle fractions of pseudo-Anosov braids (f_{pA}) evaluated at the end of the diastolic duration over 2 000 samples of random braids (i). (*b*) Convergence of the 50-particle fraction of pseudo-Anosov braids.

3. The finite-time braiding exponent (0.172 ROA)

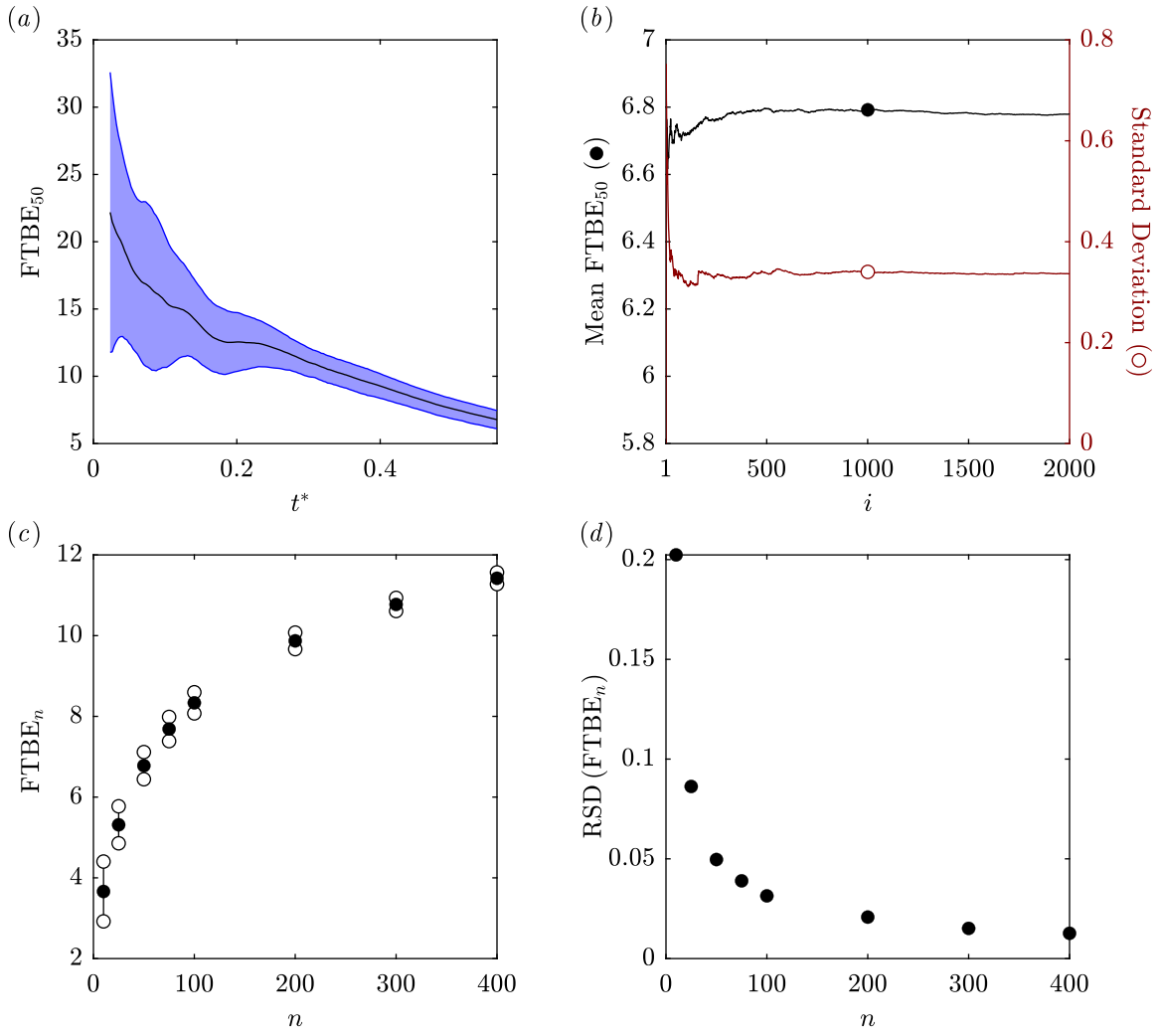

Figure S.A12: (*a*) Variation of the mean finite-time braiding exponent (FTBE) throughout the diastolic duration considering 50 particles over 2 000 sample. The lightly shaded band marks one standard deviation above and below the mean. (*b*) Variation of the mean (left axis, solid circle) and standard deviation (right axis, open circle) evaluated at the end of diastole over 2 000 samples (i). (*c*) Variation of the mean (solid circles) with respect to the number of particles (n) participating in the braid. For each n, the finite-time braiding exponent is evaluated at the end of the diastolic duration and considers 2 000 samples. The open circles mark one standard deviation above and below the mean. (*d*) The corresponding relative standard deviation (RSD), namely, the standard deviation normalized by the mean.

E. Severe aortic regurgitation 2 (0.261 ROA)

1. The normalized braid writhe (0.261 ROA)

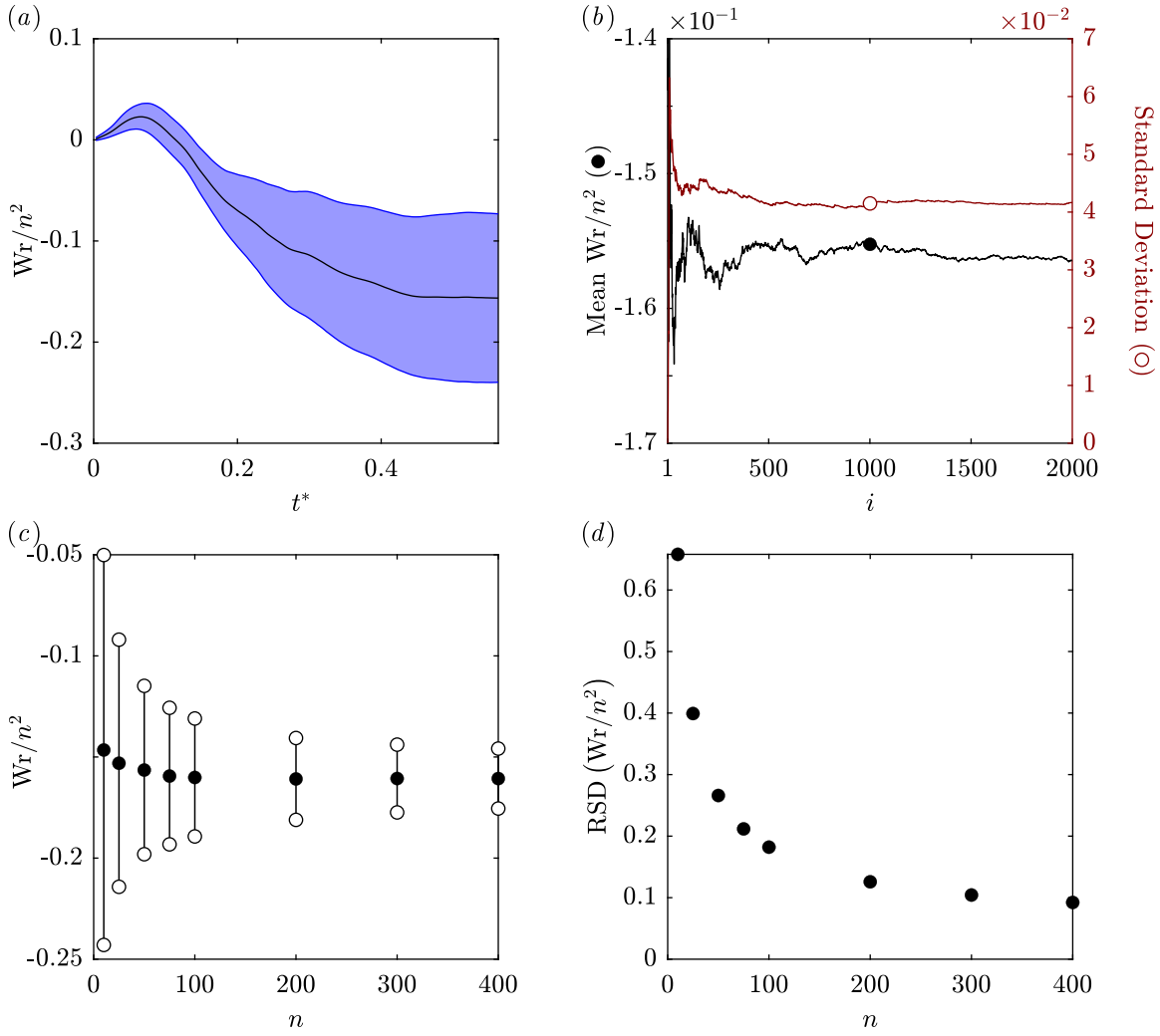

Figure S.A13: (*a*) Variation of the mean normalized writhe (Wr/n^2) throughout the diastolic duration for 50 particles over 2 000 samples. The lightly shaded band marks one standard deviation above and below the mean. (*b*) Variation of the mean (left axis, solid circle) and standard deviation (right axis, open circle) evaluated at the end of diastole over 2 000 samples (*i*). (*c*) Variation of the mean (solid circles) with respect to the number of particles (n) participating in the braid. For each n, the writhe is evaluated at the end of the diastolic duration and considers 2 000 samples. The open circles mark one standard deviation above and below the mean. (*d*) The corresponding relative standard deviation (RSD), namely, the standard deviation normalized by the mean.

2. The fraction of pseudo-Anosov braids (0.261 ROA)

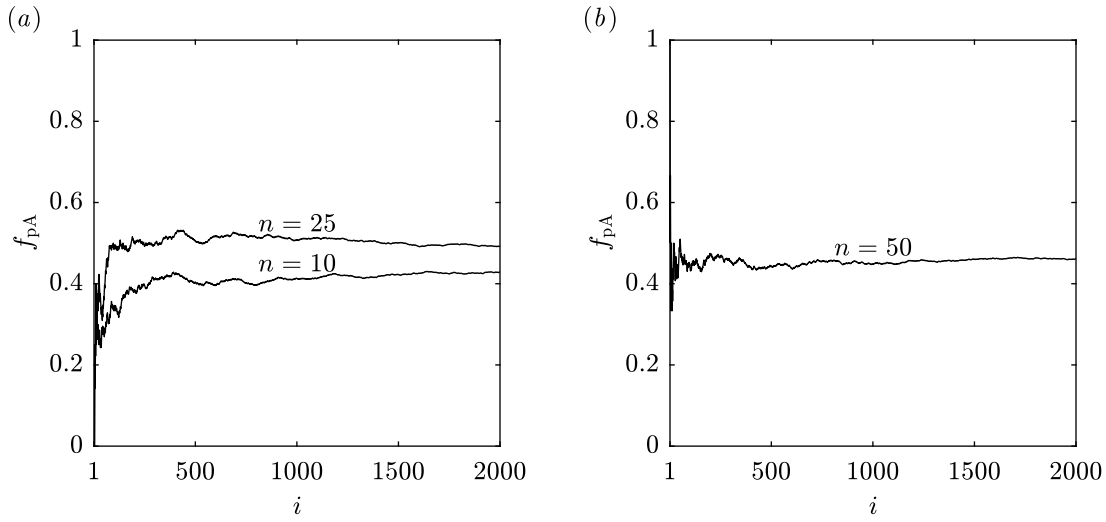

Figure S.A14: (a) Convergence of the 10- and 25-particle fractions of pseudo-Anosov braids (f_{pA}) evaluated at the end of the diastolic duration over 2 000 samples of random braids (i). (b) Convergence of the 50-particle fraction of pseudo-Anosov braids.

3. The finite-time braiding exponent (0.261 ROA)

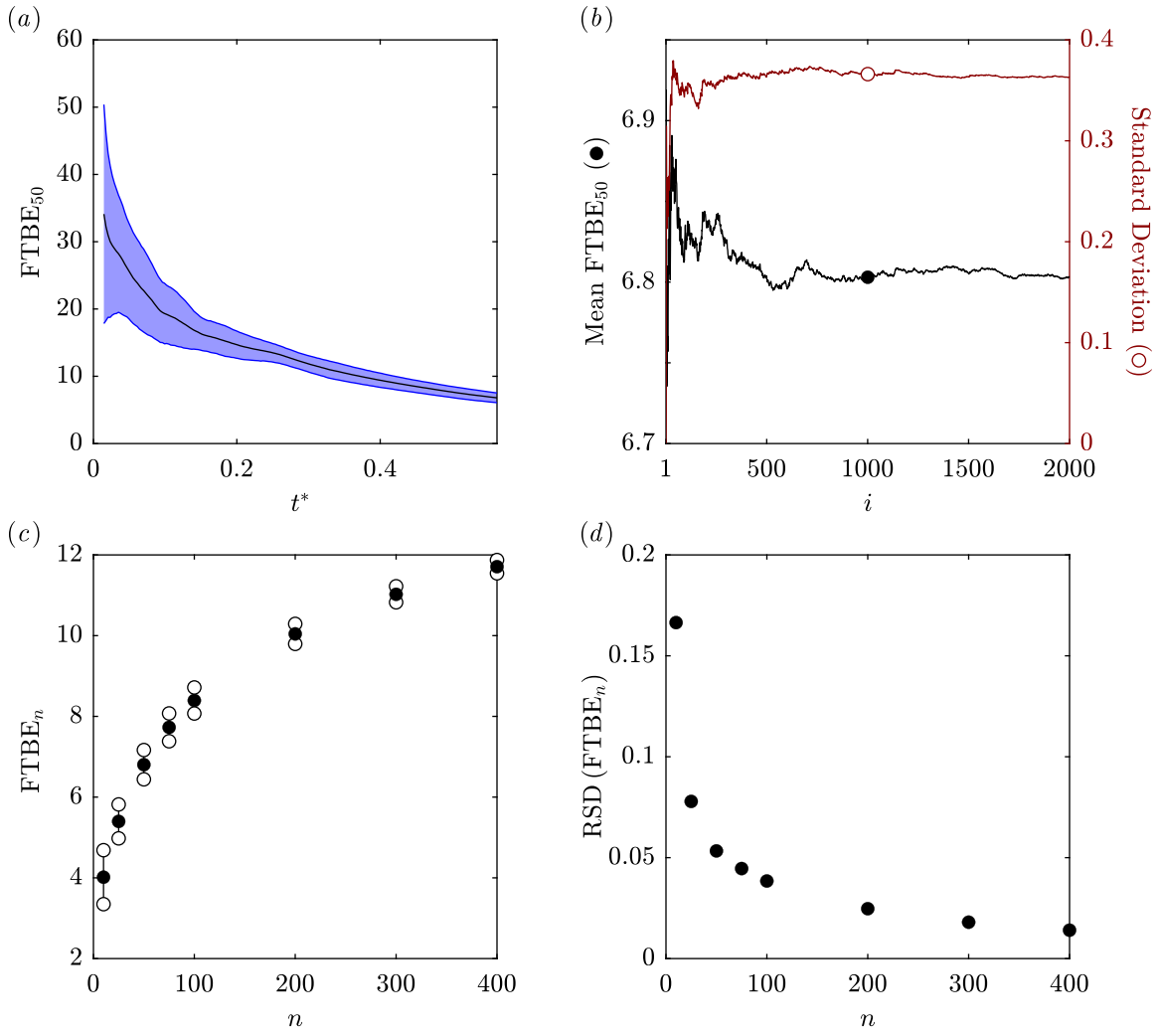

Figure S.A15: (*a*) Variation of the mean finite-time braiding exponent (FTBE) throughout the diastolic duration considering 50 particles over 2 000 sample. The lightly shaded band marks one standard deviation above and below the mean. (*b*) Variation of the mean (left axis, solid circle) and standard deviation (right axis, open circle) evaluated at the end of diastole over 2 000 samples (i). (*c*) Variation of the mean (solid circles) with respect to the number of particles (n) participating in the braid. For each n, the finite-time braiding exponent is evaluated at the end of the diastolic duration and considers 2 000 samples. The open circles mark one standard deviation above and below the mean. (*d*) The corresponding relative standard deviation (RSD), namely, the standard deviation normalized by the mean.